STRESS ANALYSIS OF A SOLID PROPELLANT ROCKET MOTOR

by

Halid Can YILDIRIM

B.S., Mechanical Engineering, Karadeniz Technical University, 2007

Submitted to the Institute for Graduate Studies in
Science and Engineering in partial fulfillment of
the requirements for the degree of
Master of Science

Graduate Program in Mechanical Engineering
Boğaziçi University

2009

STRESS ANALYSIS OF A SOLID PROPELLANT ROCKET MOTOR

APPROVED BY:

Asst. Prof. Şebnem Özüpek (Thesis Supervisor)	.....
Asst. Prof. Sami And Kılıç	.....
Assoc. Prof. Fazıl Önder Sönmez	.....

DATE OF APPROVAL: 15.06.2009

dedicated to my lovely parents

ACKNOWLEDGEMENTS

At first, I would like to thank my thesis supervisor Dr. Şebnem Özüpek for all the encouragement, foresight and relieving guidance throughout my thesis study, providing a productive and cooperative atmosphere for research. I feel lucky for being one of her students.

I would like to thank to my friends from both undergraduate and graduate studies for their friendships and supports. Also, I would like to thank to my friends who joined me in activities, such as cycling and sailing.

Special thanks to my dear H. Eda Budak for her love, support, trust, insight, patience, namely for everything that I could not remember to write right now .

I would like to thank to my elder brother Ahmet Yıldırım, for his endless support and discussions on my studies. His advices about my academic life have been useful and effective on my goals.

Finally, I would like to thank to my parents, Hatice and Yasin Yıldırım for their unlimited love and supports. I would not complete this study without their belief and trust to me. Even if they have been far from me for several years, I always feel their love.

ABSTRACT

STRESS ANALYSIS OF A SOLID PROPELLANT ROCKET MOTOR

The aim of this study is to perform structural analysis of a solid propellant rocket motor using the finite element method and to determine the effects of aging on the analysis results. Thermal and pressure loadings occurring during the firing, storing and shipping are considered to be the most critical in determining long-term behavior of the motor. Stress and strain distribution of the rocket motor under these loading conditions are determined. Maximum principal strain at the surface of the propellant and normal stresses at the interface between the liner and the insulator are evaluated as indicators of cracking in the propellant grain and debonding at the liner-insulator interface. The analyses are performed for both new and aged propellants. Analysis results are then to be used to estimate the service life of the motor.

ÖZET

KATI YAKITLI ROKET MOTORUNUN GERİLME ANALİZİ

Çalışmanın amacı, sonlu elemanlar metodunu kullanarak katı yakıtlı roket motorlarının yapısal analizini gerçekleştirmek ve yaşlanmanın analiz sonuçları üzerine etkisini belirlemektir. Motorun uzun dönemdeki davranışını belirleyici olması nedeniyle ateşleme, depolama ve taşıma sırasında oluşan sıcaklık ve basınç yükler göz önüne alınmıştır. Bu yükleme durumları altında motorun gerilme ve gerinme dağılımları belirlenmiştir. En büyük normal gerilme astar-yalıtım arayüzeyinde ayrılma açısından kritik olarak ve en büyük asal gerinim yakıt çekirdeğinde çatlak oluşumu açısından kritik olarak değerleri ve konumları belirlenmiştir. Analizler hem yaşlanmamış hem de yaşlanmış yakıt için gerçekleştirilmiştir. Analiz sonuçları daha sonra hizmet ömrü tahmininde kullanılır.

TABLE OF CONTENTS

LIST OF FIGURES

LIST OF TABLES

LIST OF SYMBOLS/ABBREVIATIONS

C_i	Temperature-dependent material parameters
D	Difference
D_i	Temperature-dependent material parameters
E_c	Elasticity modulus of FRP motor case
E_{Al}	Elasticity modulus of aluminium boss
G_0	Instantaneous modulus
G_∞	Equilibrium modulus
$\bar{I}_1$	First deviatoric strain invariant
J^{el}	Elastic volume ratio
K_0	Initial bulk modulus
N	Material constant
U	Strain Energy Function
a_T	Shift function
g_R	Dimensionless shear relaxation modulus
α_{Al}	Thermal expansion coefficient of aluminium case
α_c	Thermal expansion coefficient of FRP motor case
α_{EPDM}	Thermal expansion coefficient of EPDM
α_{pro}	Thermal expansion coefficient of propellant
τ_i^G	Material constant
θ	Temperature of the material
θ_0	Stress free temperature of the material
λ_i	principal stretches
$\bar{\lambda}_i$	Deviatoric stretches
$\dot{\varepsilon}$	Strain rate
μ_0	Initial shear modulus

CAX8H	8-node biquadratic axisymmetric quadrilateral hybrid element
FE	Finite element
FEM	Finite element method
p0	Non-pressurized analysis
p1000	Pressurized analysis

1. INTRODUCTION

Solid rocket motor consists of a solid propellant grain embedded into a stronger metallic or composite case with an insulator material between the case and the grain. The case provides the essential structural resistance against service and operational loads. Low strength of the inner propellant grain is used for transmission of loads from the grain surface to the outer case, and the insulator reduces stresses occurring in the motor.

Solid rocket motors are utilized in defence and space technologies. Motors are generally stored for a long time and/or transmitted from one place to another before their ignition processes, in other words most of their life is spent in a standby position. During their lifetime motors may encounter different environmental effects, in particular temperature variations due to change in climate of storage or regions they are transported to. Since the mechanical properties of solid propellants are very sensitive to temperature changes, the effects of thermal loads on the performance of the rocket motor should be determined. Once a motor is fired, it is impossible to put out the fire unless all of the solid propellant is consumed. Consequently, as an engineering problem motors should be carefully examined before firing.

Rocket motor should maintain its reliability and performance during its service life. In-service a rocket motor is often exposed to a wide range of thermal and pressure loading conditions which may result in stress and strain values exceeding material capabilities [1]. In that regard, as the first step to estimate the service life of the motor, critical loading conditions and failure modes should be determined. In order to accurately predict the failure mode of the motor, understanding the mechanical behavior of the grain and of the propellant-liner-insulator interfaces under several thermal and pressure loading conditions is important [1, 2]. The most common failures that occur in solid rocket motors consist of debonding at the propellant-liner or liner-insulator interface and cracking at the propellant grain. Therefore, in order to determine the service life of solid rocket motors, stresses and strains in the critical regions of the

motor should be evaluated and maximum values should be determined.

Mechanical response as well as capabilities of solid propellants may change in time. These changes are called aging, and generally result in a loss of the grain structural integrity. Aging may result from different types of processes. Chemical (i.e. oxidation, chain chissioning, incompatibilities), mechanical (i.e. thermally induced stresses, vibrations, shock loads), and physical (i.e. migration of liquid propellant components) aging are some of the most crucial ones [3]. Although the extent of these processes can partly be anticipated during design and development of the motor, the actual aging behavior is shown during in service use. The effects of aging on the critical strain and stress components should be periodically evaluated during the useful life of the motor.

In recent years, a variety of experimental and numerical works have been done to gain more information about the mechanical behavior of solid propellants and rocket motors. The mathematical description of the propellants should contain the physical and geometrical nonlinearities. Swanson and Christensen's model accounts for softening of the propellant stress-strain curve, however it assumes linear viscoelasticity [4]. The model is not suitable for representing large deformations in solid propellants, since the definitions of strain and stress deviators have physical significance only for small strains. A three dimensional finite strain viscoelastic model has been developed by Simo [5]. The most significant feature of this work is the uncoupling of volumetric and deviatoric responses over any range of deformations. Based on Simo's finite strain viscoelastic formulations Özüpek and Becker developed a phenomenological model which is applicable over any range of deformations and has an easy calibration [6, 7]. Canga *et al.* developed an efficient numerical algorithm for the model and implemented it in a finite element code [8]. For an accurate lifetime prediction of the rocket motor, aging of the propellant should also be considered. Kivity *et al.* studied the accelerated aging of propellant properties with changing percentage of integrants [9]. Heller *et al.* studied the failure of the propellant from probabilistic and chemical aging aspects [10, 11]. A methodology based on material level aging experiments in combination with computer modeling is presented by Keizers and Meidema. Several other techniques have been

used to determine the service lifetime of rocket motors. Hazim and Heller discussed service life of the motor from a numerical point of view. They also stated that during the cold days the modulus becomes higher, thus higher thermal stresses are induced, and service lives of motors are shorter at cold regions. Ho [1] evaluated the critical temperatures at which debonding and/or propellant cracking occur and the number of thermal cycles required to induce failure. Various nonlinear viscoelastic constitutive theories were studied by Collingwood *et al.* [13], and their verification in laboratory tests were performed using subscale motors. The service life estimation for a rocket motor was made assuming that only propellant capabilities changed with age. The mechanical response of the propellant was assumed to be independent of age.

Main objective of this study is to perform structural analysis of a solid rocket propellant motor using the finite element method (FEM) and determine the effects of aging on the analysis results. Loadings occurring during the firing, storing and shipping are considered to be the most critical in determining long-term behavior of the motor. Stress and strain distribution of the rocket motor under these loading conditions are determined. The maximum normal stress and maximum principal strain values and their locations are determined. The analyses are performed for both new and aged propellants. Analysis results are then to be used to estimate the service life of the motor.

In the following, the rocket motor used in this study is introduced and material properties of various motor components are presented in Chapter 2. Experimental test data and constitutive model for both new and aged propellants are described in detail. In Chapter 3, solid rocket motor analyses performed for new and aged propellants for different loading conditions are presented. In particular, maximum principal strains along the solid propellant surface and normal stresses at the interface between the liner and the insulator are calculated to determine the critical regions of the motor. Finally, summary, discussion, and future work are presented in Chapter 4.

2. THE MATERIAL MODELS

The considered solid rocket motor is composed of five different parts each with different material properties. These parts are

- Fiberglass Reinforced Plastic (FRP) Motor Case
- Aluminum Boss
- EPDM[1] Insulator
- Liner
- Solid Propellant

A section view of the motor is illustrated in Figure 2.1. The inner and the main part of the motor is an HTPB[2] based propellant, and surrounding outer portion is the case. The insulation is located between the case and the liner covering the solid propellant. Case provides the essential structural resistance with its reinforced strength. Aluminum bosses are located at the top and the bottom of the motor to support the structure. Two features of the motor design aim to release the stresses. One is the slot at the top of the motor, another is the free flap within the insulator at the bottom of the motor.

In the stress analysis, both FRP motor case and aluminum boss are modeled as linear-elastic. Whereas, liner and solid propellant are modeled as viscoelastic, and EPDM as a hyperelastic material.

In this section, mechanical properties of materials used in this study are presented, and the implementation of these materials into ABAQUS is discussed.

[1]Ethylene Propylene Diene M-Class Rubber.
[2]Hydroxyl Terminated PolyButadien

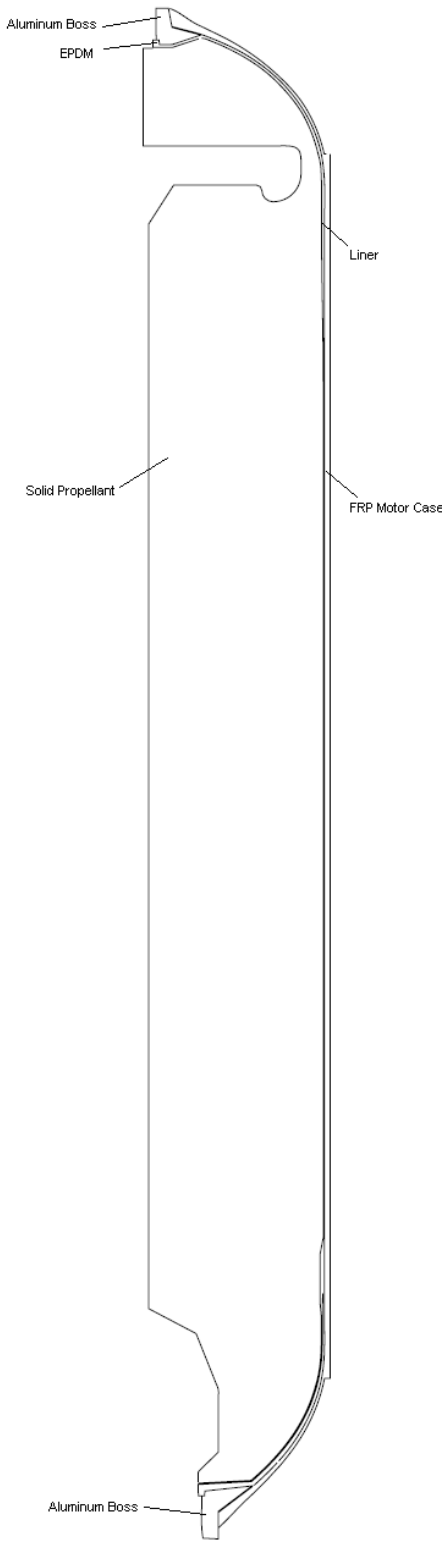

Figure 2.1. A section view of solid rocket motor

2.1. Mechanical Properties of Materials

2.1.1. FRP Motor Case

FRP rocket motor case is modeled as a linear-elastic material with the following elasticity modulus, E, Poisson's ratios, ν, thermal expansion coefficient, α, and reference temperature, θ_0:

$$\begin{aligned} E_c &= 4615.3 kg/mm^2,\ \nu_c = 0.33 \\ \alpha_c &= 2.304{\times}10^{-6^\circ} C^{-1},\ \theta_0 = 20^\circ C \end{aligned} \tag{2.1}$$

2.1.2. Aluminum Boss

Aluminum boss is considered as a linear-elastic material with the following material properties

$$\begin{aligned} E_{Al} &= 7031 kg/mm^2,\ \nu_{Al} = 0.33 \\ \alpha_{Al} &= 22.5{\times}10^{-6^\circ} C^{-1},\ \theta_0 = 20^\circ C \end{aligned} \tag{2.2}$$

2.1.3. EPDM Insulation

EPDM, insulation material, is modeled as a hyperelastic material. Hyperelastic materials are described in terms of a strain energy potential, $U(\varepsilon)$, which defines the strain energy stored in the material per unit of reference volume (volume in the initial configuration) as a function of the strain at that point in the material. Neo-Hookean formulation of the strain energy potentials is considered for EPDM [15].

$$U = C_{10}(\bar{I}_1 - 3) + \frac{1}{D_1}(J^{el} - 1)^2 \tag{2.3}$$

where U is the strain energy per unit of reference volume; C_{10} and D_1 are the temperature dependent material parameters; $\bar{I}_1$ is the first deviatoric strain invariant defined as

$$\bar{I}_1 = \bar{\lambda_1}^2 + \bar{\lambda_2}^2 + \bar{\lambda_3}^2 \tag{2.4}$$

$$\bar{\lambda}_i = J^{\frac{-1}{3}} \lambda_i \tag{2.5}$$

where $\bar{\lambda}_i$ are the deviatoric stretches, J is the total volume ratio, J^{el} is the elastic volume ratio and λ_i are the principal stretches. The initial shear modulus and bulk modulus are given by

$$\begin{aligned} \mu_0 &= 2C_{10} \\ K_0 &= \frac{2}{D_1} \end{aligned} \tag{2.6}$$

Equation 2.6 represents the actual way of implementing bulk modulus into ABAQUS when hyperelastic material model is used. Mechanical properties of the insulation material are

$$\begin{aligned} C_{10} = 0.05 kg/mm^2,\ K_0 = 200 kg/mm^2 \\ \alpha_{EPDM} = 1.8{\times}10^{-6^\circ} C^{-1},\ \theta_0 = 60^\circ C \end{aligned} \tag{2.7}$$

2.1.4. Solid Propellant

Solid propellants use an elastomeric binder that is filled with a high level of solid particles, such as oxidizer crystals and fuel. Some ingredients, such as curing agents and burn-rate catalysts are added to the propellant to improve the rheological and physical properties, to optimize the burn rate and to improve bonding [6]. Different mechanisms

may occur in the solid propellants when the load is applied. As a result of these, propellants exhibit large deformation and large strains, rapid decrease of stress during unloading, large hysteresis during cyclic loading, and transition from incompressible to compressible behavior at the onset of damage [7]. A constitutive model representing these effects was proposed in [8]. Although the model is calibrated for the rocket motor propellant used in this study [17], its implementation in ABAQUS is not yet available. Therefore, the stress analysis was done using the finite strain viscoelastic model available in ABAQUS.

Propellants at two different ages are considered for the structural analysis: the "new" propellant is newly cured, the "aged" propellant is six years older than the new one.

2.1.4.1. New Propellant. Finite strain viscoelastic representation combines viscoelasticity with a hyperelastic model. A reduced polynomial form, in particular Yeoh model [16], is selected for the hyperelastic part. Yeoh states the strain energy function in the form of

$$U = C_{10}(\bar{I}_1 - 3) + C_{20}(\bar{I}_1 - 3)^2 + C_{30}(\bar{I}_1 - 3)^3 + \frac{1}{D_1}(J^{el} - 1)^2 \tag{2.8}$$

where C_{i0}, D_1, and J^{el} are as stated in Section 2.1.3. The coefficients of U in Equation 2.8 were found by fitting the constitutive model prediction to uniaxial constant strain rate test data with superimposed pressure corresponding to the highest pressure the propellant is exposed to. This test is assumed to represent material response without damage. The coefficients are given in Table 2.1.

The viscoelastic material property is defined by a relaxation modulus. Prony series expansion is used to represent the dimensionless shear relaxation modulus

$$g_R(t) = 1 - \sum_{i=1}^{N} \bar{g_i}^P (1 - e^{-t/\tau_i^G}) \tag{2.9}$$

where N, $\bar{g}_i{}^P$, and τ_i^G are material constants.

Stress response of a viscoelastic material depends on strain rate. It was stated in Özüpek and Becker's study [7] that for most propellants dilatation has little rate dependence at constant strain rate tests and no measurable time dependence at relaxation tests. Therefore, dilatation is considered as rate independent, so volumetric behavior is also viscoelastic. In this study, same relaxation function as given in Equation 2.9 is used for the volumetric response. The relaxation curve for the new propellant is shown in Figure 2.2, and the normalized prony series coefficients are given in Table 2.2. The equilibrium modulus, G_∞, and the instantaneous modulus, G_0, are

$$\begin{aligned} G_\infty &= 1.17 \times 10^{-1}\ kg/mm^2 \\ G_0 &= 6.507\ kg/mm^2 \end{aligned} \tag{2.10}$$

Since Equation 2.9 is dimensionless, hyperelastic coefficients C_{i0} are multiplied by the instantaneous shear modulus, as given in Table 2.1.

Table 2.1. Hyperelastic coefficients of new propellant

Coefficient	kg/mm^2	multiplied by G_0
C_{10}	3.7694×10^{-1}	2.452949791
C_{20}	1.3243×10^{-1}	0.861792701
C_{30}	-1.8037×10^{-1}	-1.17376387

In this study, the dependence of viscoelastic properties on temperature changes is defined by a shift factor determined from several relaxation test data of the propellant. The shift function, a_T, was represented in WLF form, as proposed by Williams *et al.* [18]

$$\log a_T = -\frac{C_1(\theta - \theta_0)}{C_2 + (\theta - \theta_0)} \tag{2.11}$$

Table 2.2. Normalized prony series of new propellant

N	$\bar{g}_i^P$	$\bar{k}_i^P$	τ_i^G, minute
1	0.31686350	0.31686350	1×10^{-6}
2	0.36025936	0.36025936	1×10^{-5}
3	0.16311863	0.163118630	1×10^{-4}
4	0.07820935	0.07820935	1×10^{-3}
5	0.02805517	0.02805517	1×10^{-2}
6	0.01822964	0.01822964	1×10^{-1}
7	0.00957705	0.00957705	1
8	0.00535763	0.00535763	$1\times10^{+1}$
9	0.00041825	0.00041825	$1\times10^{+2}$
10	0.0019107	0.00191071	$1\times10^{+3}$

where θ_0 is the reference temperature, and C_1, C_2 are material constants. Equation 2.11 has been used to describe the temperature effect on the relaxation behavior of many polymers with fairly satisfactory results [19]. The coefficients of the shift function for the new propellant are

$$\begin{aligned} \alpha_{pro} &= 0.87\times10^{-4^\circ}C^{-1} \\ \theta_0 &= 60^\circ C \\ C_1 &= 4.74 \\ C_2 &= 210.47^\circ C \end{aligned} \tag{2.12}$$

The prediction of the new constitutive model described above and the experimental data for the uniaxial constraint strain rate loading are shown in Figure 2.3. The experimental test data was obtained from non-pressurized and pressurized experiments [17]. The non-pressurized test data was obtained from a simple uniaxial test, whereas the pressurized test data was obtained from a simple uniaxial test with a chamber pressure of $0.6895kg/mm^2(980.7psi)$. As can be seen from Figure 2.3, non-pressurized and pressurized test data curves overlap up to the value of nearly 0.1 strain. After

that value, the difference of non-pressurized and pressurized test data increases due to damage effect in the solid propellant. The finite strain viscoelastic model used in this study is a non-damaging model, therefore the predictions for both pressure levels overlap as seen in Figure 2.3. Further discussion regarding the new propellant model is given in Section 2.1.4.4.

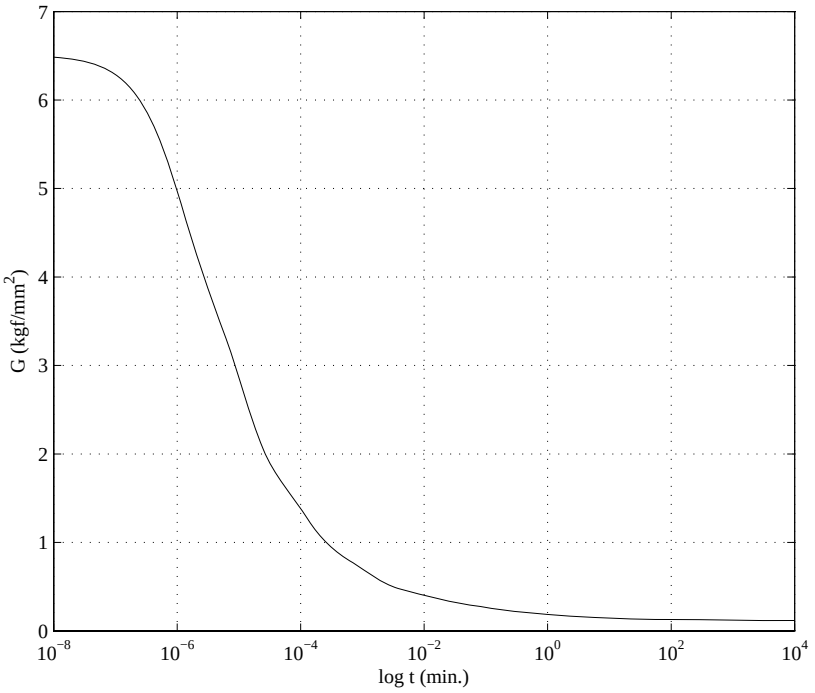

Figure 2.2. The relaxation curve of new propellant

2.1.4.2. Aged Propellant. The service life prediction of the rocket motor requires the determination of aging trends of the propellant behavior. On the other hand, experiments and observations of aged propellants are very limited due to lack of naturally aged propellant availability. In this study limited data for a six year old propellant was available [17].

The Yeoh form of strain energy potential used for the new propellant was not used for the aged propellant since uniaxial test data with a pressure level high enough to assume no damage was not available. Instead, Neo-Hookean strain energy potential

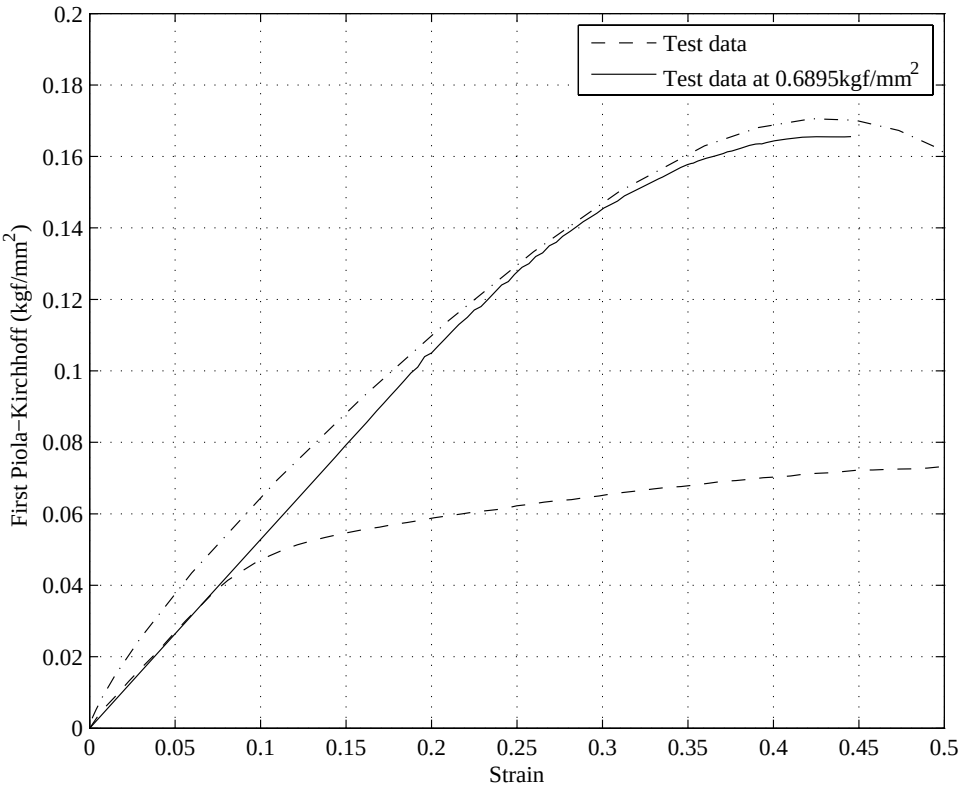

Figure 2.3. Comparison of ABAQUS model with non-pressurized and pressurized test data for new propellant ($\dot{\varepsilon} = 0.7291[1/min]$)

$$U = C_{10}(\bar{I}_1 - 3) + \frac{1}{D_1}(J^{el} - 1)^2 \tag{2.13}$$

was used with C_{10}, D_1, and J^{el} as stated in Section 2.1.3. The hyperelastic coefficient C_{10} was fitted to the uniaxial test data up to onset of damage, about 0.1 strain level [17]. The resulting coefficient is shown in Table 2.3.

Table 2.3. Hyperelastic coefficient of aged propellant

Coefficient	kg/mm^2	multiplied by (G_0)
C_{10}	3.1691×10^{-1}	2.444

The relaxation curve for the aged propellant is shown in Figure 2.4, and the normalized prony series coefficients are given in Table 2.4.

Table 2.4. Normalized prony series of aged propellant

N	$\bar{g}_i{}^P$	$\bar{k}_i{}^P$	τ_i^G, minute
1	0.41988643	0.41988643	1×10^{-6}
2	0.22904074	0.22904074	1×10^{-5}
3	0.15027800	0.15027800	1×10^{-4}
4	0.04890939	0.04890939	1×10^{-3}
5	0.04361316	0.04361316	1×10^{-2}
6	0.00839941	0.00839941	1×10^{-1}
7	0.02066500	0.02066500	1
8	0.01343698	0.01343698	$1\times10^{+1}$
9	0.01219195	0.01219195	$1\times10^{+2}$
10	0.00645608	0.00645608	$1\times10^{+3}$

The equilibrium and instantaneous modulus for the aged propellant are presented

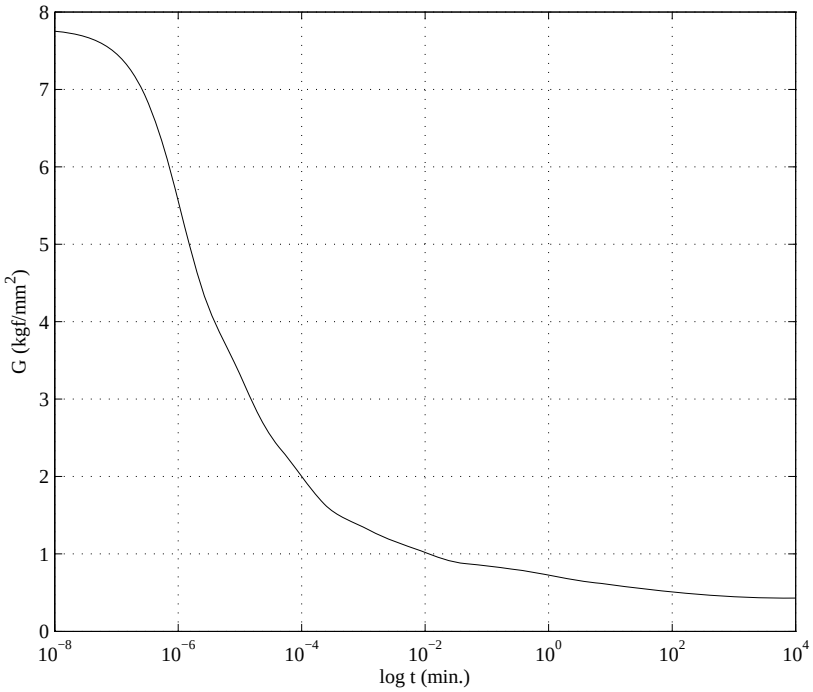

Figure 2.4. The relaxation curve of aged propellant

in Equation 2.14.

$$\begin{aligned} G_\infty &= 3.63 \times 10^{-1}\ kg/mm^2 \\ G_0 &= 7.713\ kg/mm^2 \end{aligned} \tag{2.14}$$

The coefficients of shift function 2.11 for the aged propellant are

$$\begin{aligned} \alpha_{pro} &= 0.87{\times}10^{-4^\circ}\frac{1}{C} \\ \theta_0 &= 60^\circ C^{-1} \\ C_1 &= 9.065 \\ C_2 &= 275.58^\circ C \end{aligned} \tag{2.15}$$

The prediction of the aged constitutive model described above and the experimental data for the uniaxial constraint strain rate loading are shown in Figure 2.5.

The experimental data was obtained from non-pressurized and pressurized tests [17]. The non-pressurized experimental test data was obtained from a simple uniaxial test, whereas the pressurized test data was obtained from a simple uniaxial test with a chamber pressure of $0.281 kg/mm^2 (400 psi)$ [17]. Available test data of the aged propellant is compared with the response of the FE simulation. Since the finite strain viscoelastic model used in this study is a non-damaging model, the predictions for both pressure levels overlap as seen in Figure 2.5.

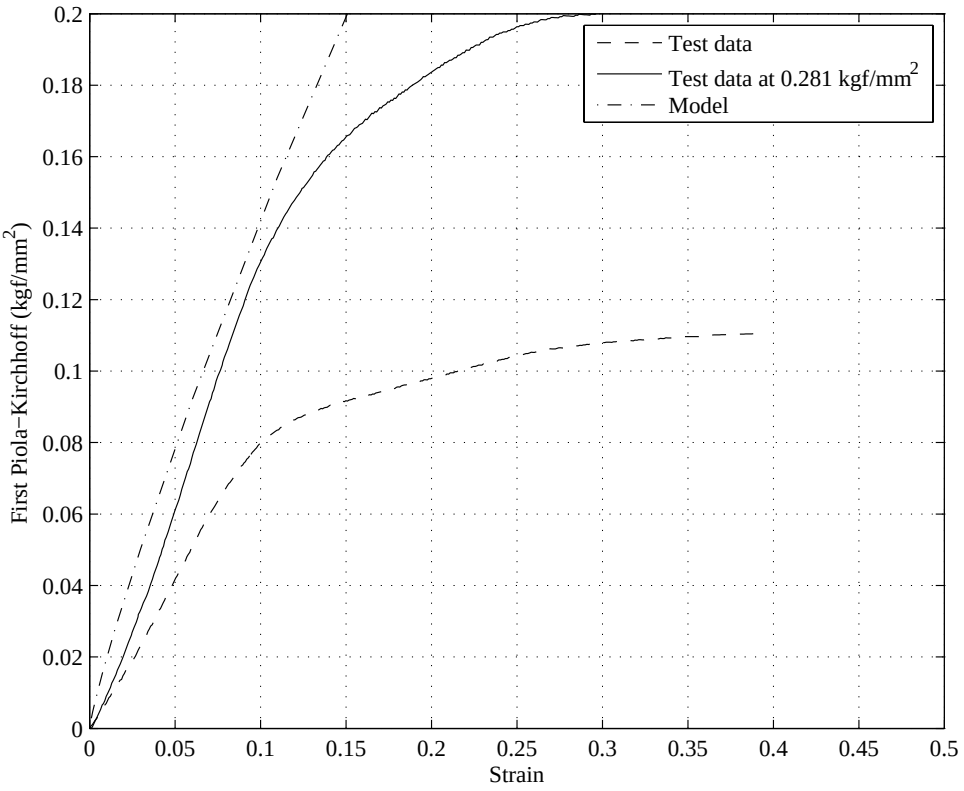

Figure 2.5. Comparison of ABAQUS model with non-pressurized and pressurized test data for aged propellant ($\dot{\varepsilon} = 0.7291[1/min]$)

It is observed from Figure 2.5 that initial slopes of non-pressurized and pressurized test data are distinct, contrary to that of the new propellant where pressure has not effect up to 0.1 strain, where material starts softening due to damage. Due to limited data for aged propellant, more definite conclusion regarding the initial slope could not be made. Further comments regarding the aged propellant are presented in Section 2.1.4.4.

2.1.4.3. Aging effects. In order to clearly see the effect of aging the relaxation moduli for the new and aged propellant are compared in Figure 2.6. Higher modulus for the aged propellant indicates its stiffened behavior. This can be also observed in Figure 2.7 where uniaxial response of the propellants are compared. Test data states that aged propellant is stiffer than the new one, and the same behavior is represented in the constitutive models. The maximum strain predictions for the aged propellant are expected to be lower than those for the new one, while maximum stress predictions are expected to be higher.

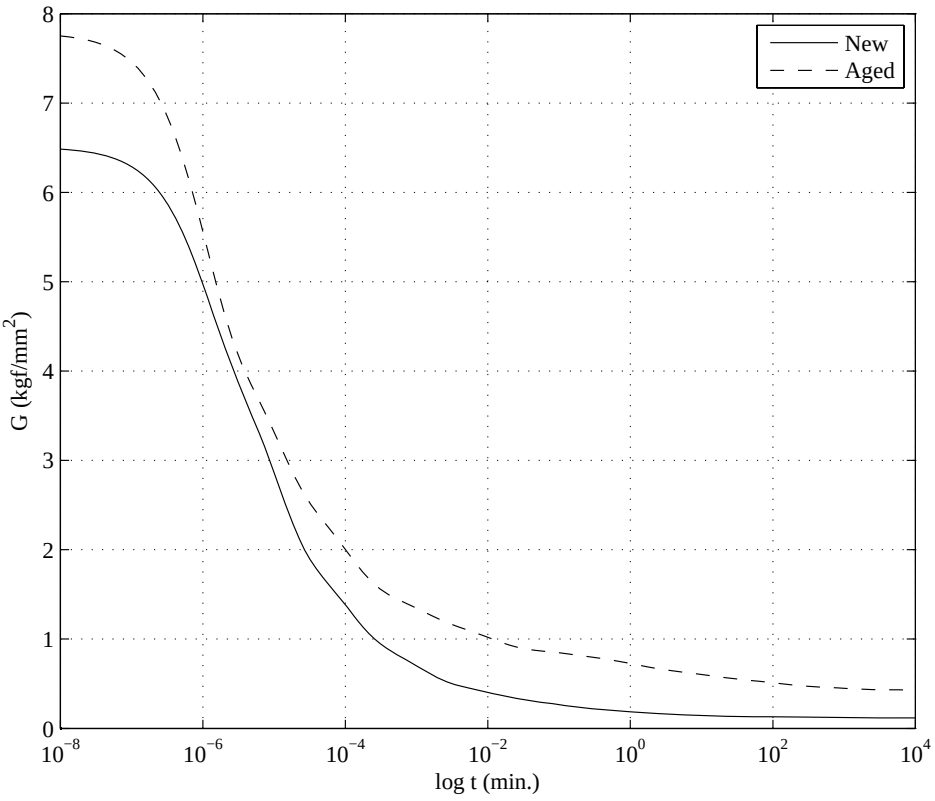

Figure 2.6. Comparison of relaxation curves for new and aged propellant

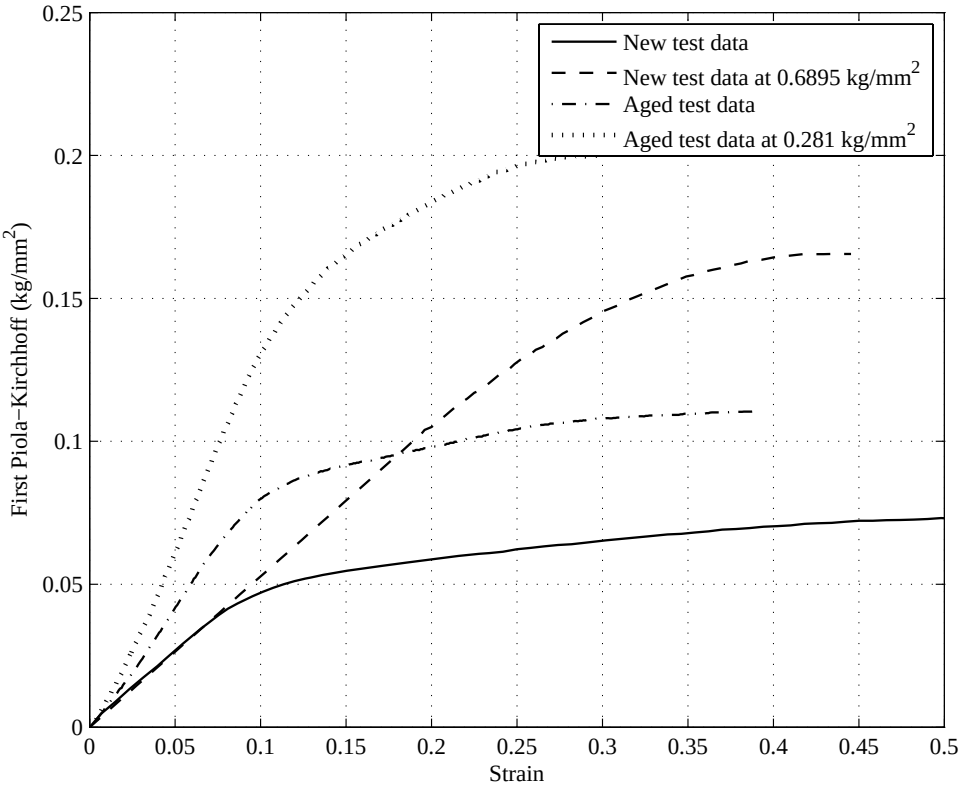

Figure 2.7. Uniaxial constant strain rate test data ($\dot{\varepsilon} = 0.7291[1/min]$)

2.1.4.4. Discussion on Propellant Models. Solid propellants have different responses when uniaxial tests are performed in pressurized and non-pressurized (ambient pressure) environments (see Figure 2.7). The stress-strain curves overlap while the propellant remains incompressible. Once dilatation starts the stress response softens. The softening, referred to as damage, is suppressed at high pressure levels. When general loading conditions are considered, it is important to account for the softening, i.e. damage, in the constitutive model of the propellant. For the loadings analyzed in this work, however, the use of a non-damaging model is acceptable.

It is expected that for thermal loads maximum strain will not exceed the value of 0.1. For pressure loads this value may be exceeded, hence it is reasonable to use a model that was fitted to pressurized test data (Figure 2.3).

For the aged propellant, test data at a pressure level high enough to suppress dilatation was not available. Furthermore, the initial slope of stress-strain curve was different for two available pressure levels. Due to lack of limited data and for consistency in the calibration of the propellant model only the pressurized test data was used in the determination of the hyperelastic coefficient of the aged propellant.

3. THE SOLID ROCKET MOTOR ANALYSIS

The main aim of this study is to perform the finite element analysis of the new and aged solid propellants under various conditions to determine the critical loading and the corresponding stress and strain levels that cause the failure of the motor. Typically, the rocket motor reaches the end of its service life as a result of crack formation in the grain, or debonding at the liner-insulation interface, that is when maximum strain or stress exceed the corresponding material capacity or strength, respectively. Loadings that were analyzed in this study represent the launching of the rocket, the storage and transmission of the rocket motor. All analyses were performed in finite element package ABAQUS [20]. Since the considered rocket motor is small enough, the gravitational force is not very significant in this study.

3.1. The Finite Element Model

The finite element mesh was previously constructed with the finite element package TEXPAC [8]. In order to transfer the mesh into ABAQUS, an interface code was developed in MATLAB. Assignment of material properties to elements was completed in ABAQUS.

The finite element mesh of the rocket motor can be seen in Figure 3.1. For all loadings axisymmetric analysis was performed. The mesh consisted of 4973 nodes, and 1314 8-node biquadratic axisymmetric quadrilateral hybrid elements (CAX8H). The term “hybrid” refers to the assumption of fully incompressible material. Steps, temperature and pressure conditions are defined for each particular loading case separately. Section views of rocket motor for each part are illustrated in Appendix A.

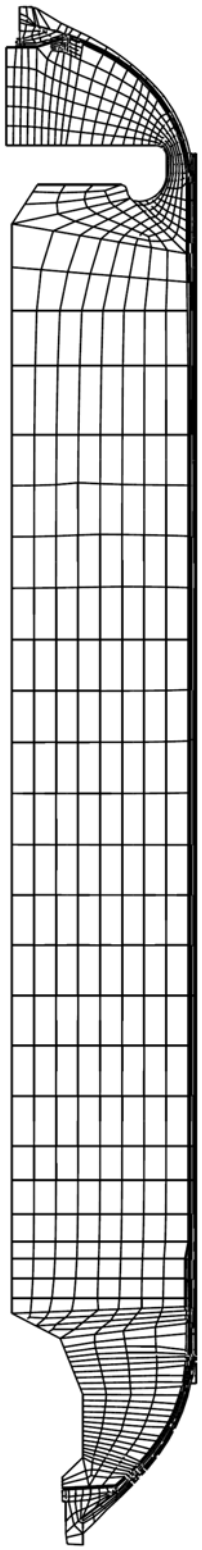

Figure 3.1. Meshed view of rocket motor in ABAQUS CAE

The service life prediction requires an accurate determination of critical regions. In order to determine the critical locations for the formation of crack or initiation of debonding the following regions of the motor are examined for the distribution of bond stress and hoop strain, the maximum principal strain.

Table 3.1. Critical regions of the rocket motor

Prop top is the top center line of the propellant (Figure 3.2)
Slot x at the top curvature of the propellent (Figure 3.3)
Slot b at the top horizontal segment of the propellent (Figure 3.4)
Bore x in the center line of the propellant (Figure 3.5)
Bond h between the liner and EPDM at the top of the motor (Figure 3.6)
Bond x between the liner and EPDM at the middle of the motor (Figure 3.7)

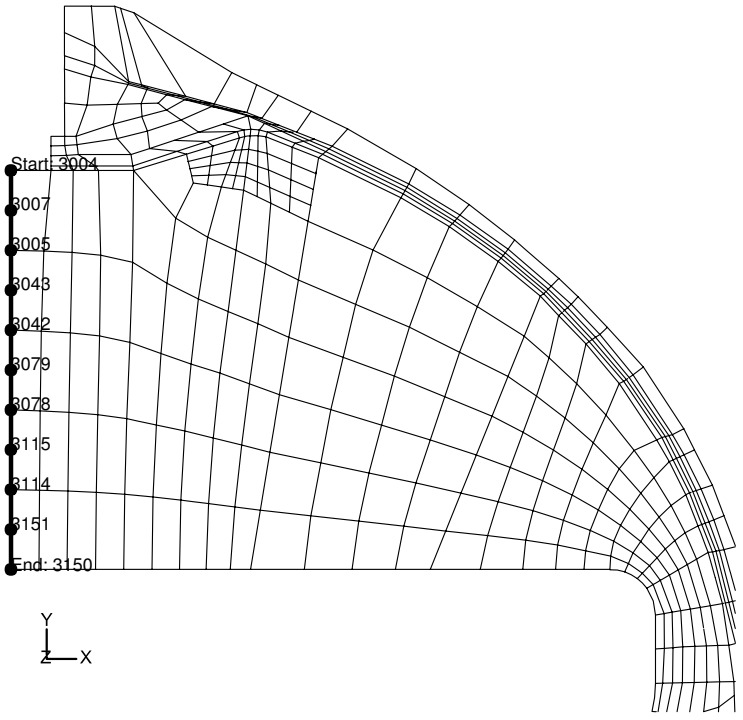

Figure 3.2. Propellant Top View (Prop top)

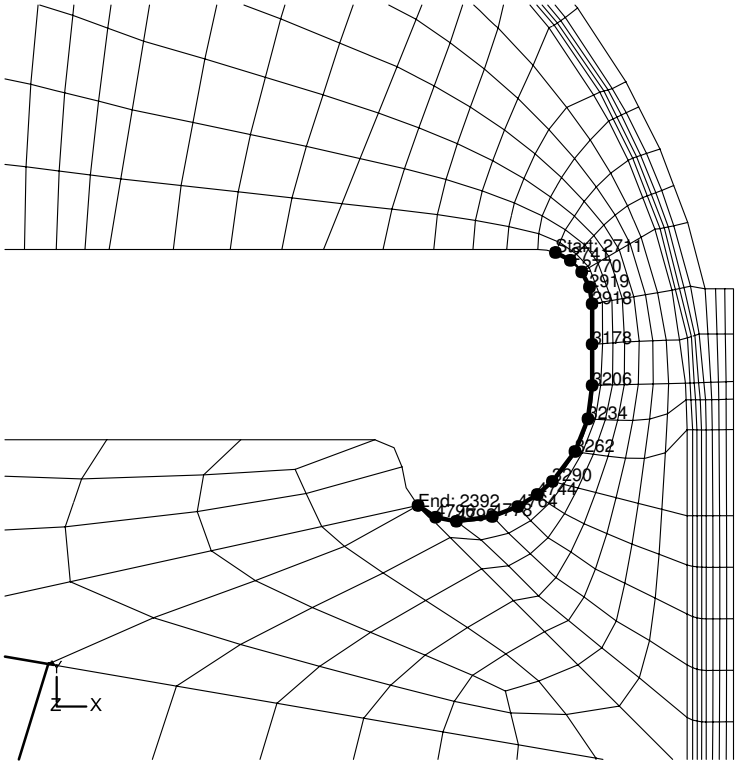

Figure 3.3. Slot View (Slot x)

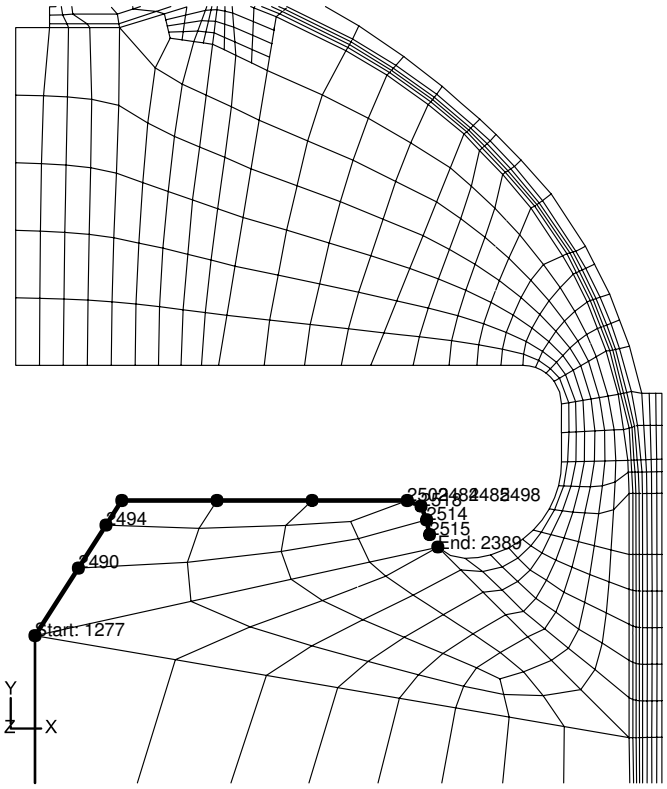

Figure 3.4. Slot View (Slot b)

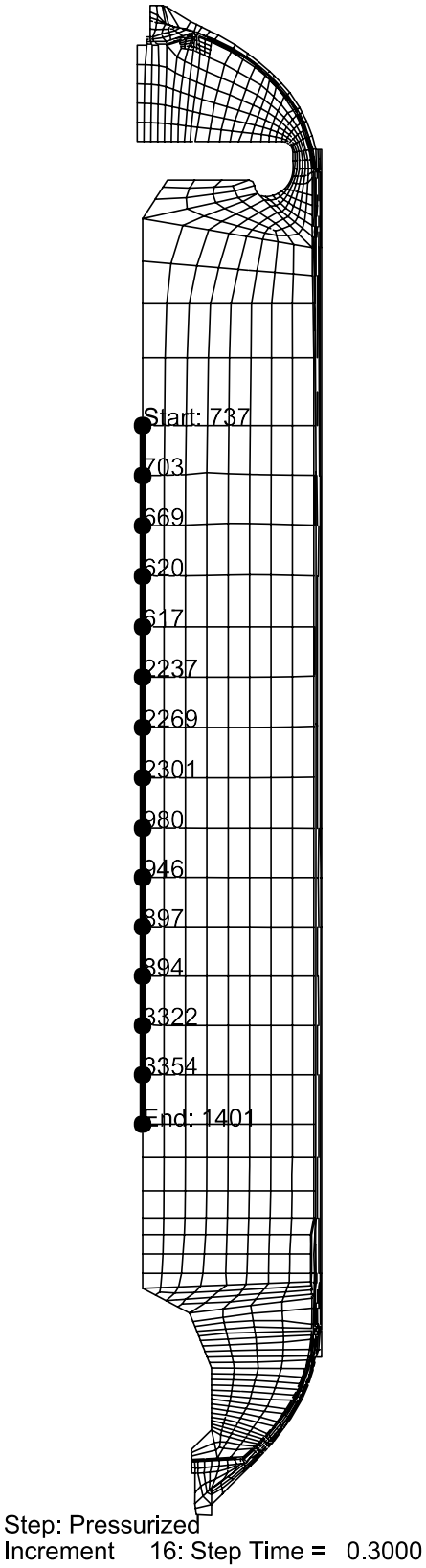

Figure 3.5. Bore View (Bore x)

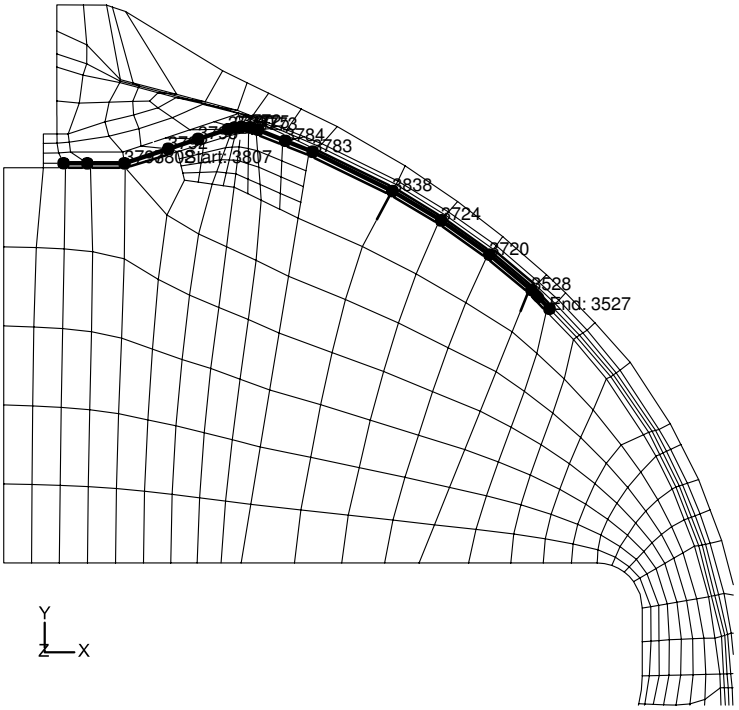

Figure 3.6. Slot View (Bond h)

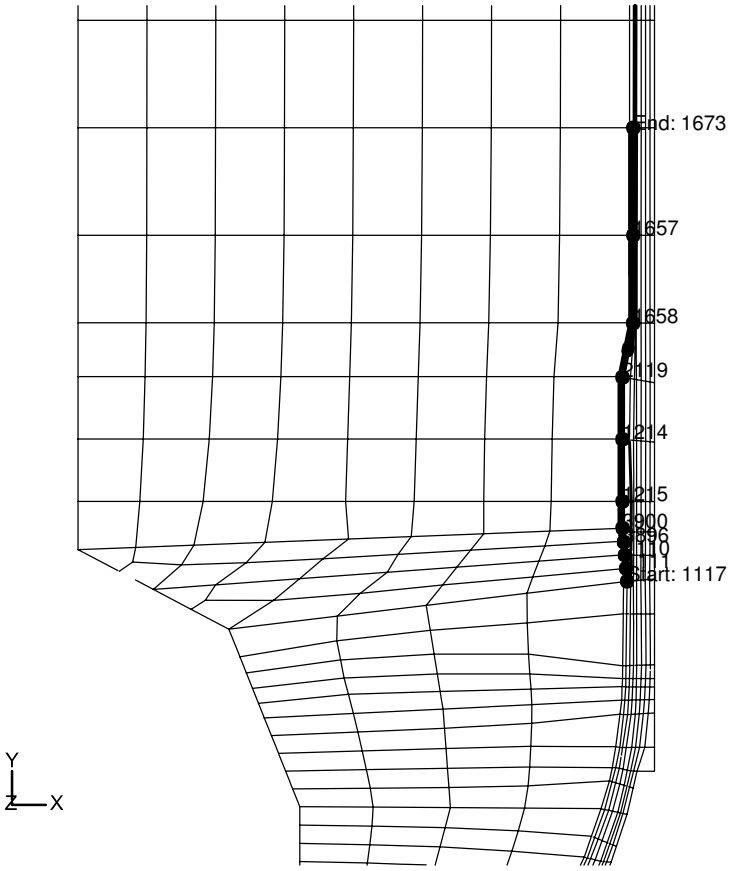

Figure 3.7. Bond View (Bond x)

3.2. Finite Element Analysis

Finite element analysis was done for three loadings. Ignition pressurization (Section 3.2.1) represents the launching of the rocket and may induce significant stresses due to low stiffness of the FRP case. Thermal cycling (Section 3.2.2) represents worst temperature conditions the motor may be subjected to during its service life. Thermal storage (Section 3.2.3) represents average temperature variations during one year while the motor is stored.

3.2.1. Ignition Pressurization Analysis

There are three loading steps in the analysis. First two steps correspond to the cooling down of the propellant, and last step corresponds to the ignition pressurization. First step is defined as one day cooling from $60°C$ to $-20°C$ followed by another step for four days of cooling to $-32°C$ as shown in Figure 3.8. The last step is ignition pressurization to 0.654 kg/mm^2 (943 psi) with a rise time of 0.3 seconds. In order to alleviate the convergence, equal increments are considered for the cooldown steps. On the other hand, automatic time intervals are appropriate for the pressure analysis.

Steps for ignition pressurization analysis are taken as

- *Cooldown 1:* 40 increments to 86400 seconds ($60°C$ to $-20°C$)
- *Cooldown 2:* 40 increments to 432000 seconds ($-20°C$ to $-32°C$)
- *Pressure:* 16 increments to 432000.3 seconds ($0.654 kg/mm^2$)

Figures 3.9 to 3.14 show results after cooldown and ignition pressurization analysis for regions identified in Table 3.1. Results for the new and aged propellants are plotted for each region. Maximum principal strain and bond stress values and their locations are given in Table 3.2 and 3.3 for new and aged propellants, respectively. As stated previously, maximum principal strain, ε, is critical for prop top, bore x, slot b, and slot x regions, whereas normal stress, σ, is critical for bond h and bond x regions. Table 3.4 compares calculated values for new and aged propellants. Differences, D,

between new and aged propellant are also indicated in Table 3.4. Difference is defined as

$$D = \frac{New - Aged}{New} \times 100 \tag{3.1}$$

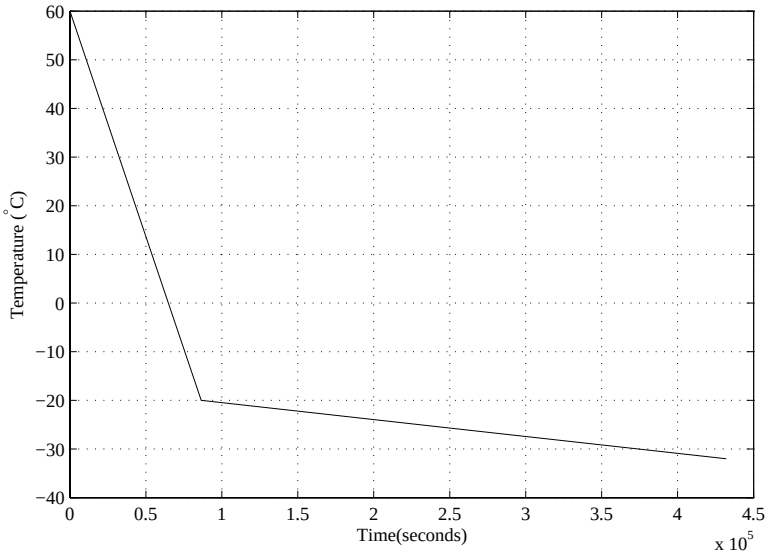

Figure 3.8. Propellant temperature history for ignition pressurization

Maximum principal strains can be readily obtained from the finite element program. However, the normal stresses or bond stresses need to be calculated as a post-processing operation. In order to obtain normal stresses between the liner and the insulator, element by element coordinate transformations are performed, and the resulting Cauchy stresses are averaged for the nodes that belong to more than one element.

According to Table 3.4, maximum principal strains for the aged propellant are slightly lower then those for the new propellant. This is expected, since the material response shown in Figure 2.7 states that aged propellant has a stiffer behavior than the new one, therefore strain values obtained from the new model will be greater than those obtained from the aged one. Maximum normal stresses for the aged propellant are much greater than those for the new one. Figure 2.7 also verifies this result. The rigidity of the material does not allow large strains for the aged propellant, therefore

stress response of the aged one is higher.

Maximum principal strain of 1.39×10^{-1} occurs at the middle surface of the propellant grain at the end of pressurization analysis (Figure 3.10). Whereas, maximum normal stress of $6.50\times10^{-2} kg/mm^2$ is calculated between the liner and the insulator at the tip of the free flap. (Figures 3.13 and 3.14).

Table 3.2. Maximum principal strains and normal stresses for new propellant and their locations for ignition pressurization analysis

Location	Step	Element(s)	Node	Hoop Strain	Bond Stress
					kg/mm^2
Prop top	Cooldown	923	3150	2.30×10^{-2}	-
	Pressurization	923	3150	3.69×10^{-2}	-
Bore x	Cooldown	712, 840	2269	9.25×10^{-2}	-
	Pressurization	712, 840	2269	1.39×10^{-1}	-
Slot b	Cooldown	371, 372, 642	1277	2.55×10^{-2}	-
	Pressurization	371, 372, 642	1277	4.61×10^{-2}	-
Slot x	Cooldown	1125, 1292	3290	6.90×10^{-2}	-
	Pressurization	817, 1047	2770	1.19×10^{-1}	-
Bond h	Cooldown	1236, 151	3772	-	6.90×10^{-3}
	Pressurization	1236, 151	3772	-	-6.94×10^{-1}
Bond x	Cooldown	526, 322	3900	-	2.43×10^{-2}
	Pressurization	322	3901	-	-6.89×10^{-1}

Table 3.3. Maximum principal strains and normal stresses for aged propellant and their locations for ignition pressurization analysis

Location	Step	Element(s)	Node	Hoop Strain	Bond Stress
					kg/mm^2
Prop top	Cooldown	923	3150	2.29×10^{-2}	-
	Pressurization	923	3150	3.58×10^{-2}	-
Bore x	Cooldown	712, 840	2269	8.92×10^{-2}	-
	Pressurization	712, 840	2269	1.29×10^{-1}	-
Slot b	Cooldown	371, 372, 642	1277	2.49×10^{-2}	-
	Pressurization	371, 372, 642	1277	4.37×10^{-2}	-
Slot x	Cooldown	1125, 1292	3290	8.36×10^{-2}	-
	Pressurization	817, 1047	2770	1.22×10^{-1}	-
Bond h	Cooldown	1236, 151	3772	-	2.13×10^{-2}
	Pressurization	1236, 151	3772	-	-7.11×10^{-1}
Bond x	Cooldown	526, 489	1215	-	6.50×10^{-2}
	Pressurization	322	3901	-	-7.09×10^{-1}

Table 3.4. Maximum principal strains and maximum normal stresses after cooldown and pressure steps for ignition pressurization analysis

Step:	Cooldown			Pressure		
Model:	New	Aged	D	New	Aged	D
Prop top, ε	2.30×10^{-2}	2.29×10^{-2}	0.43%	3.69×10^{-2}	3.58×10^{-2}	2.98%
Bore x, ε	9.25×10^{-2}	8.92×10^{-2}	3.28%	1.39×10^{-1}	1.29×10^{-1}	5.36%
Slot b, ε	2.55×10^{-2}	2.49×10^{-2}	2.35%	4.61×10^{-2}	4.37×10^{-2}	5.2%
Slot x, ε	8.39×10^{-2}	8.36×10^{-2}	0.46%	1.19×10^{-1}	1.22×10^{-1}	7.9%
Bond h, σ	6.9×10^{-3}	2.13×10^{-2}	208%	-6.94×10^{-1}	-7.11×10^{-1}	3.28%
Bond x, σ	2.43×10^{-2}	6.50×10^{-2}	167%	-6.89×10^{-1}	-7.09×10^{-1}	2.82%

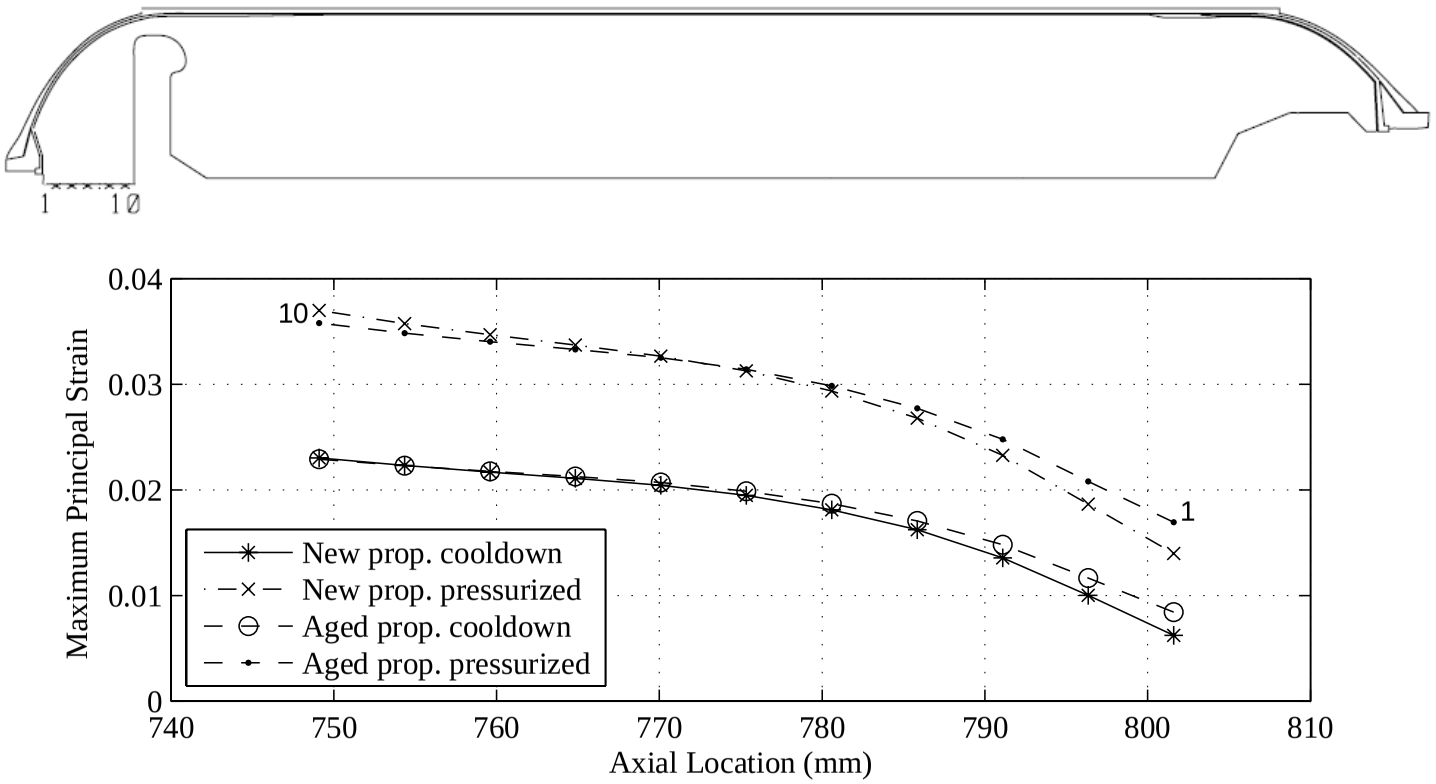

Figure 3.9. Maximum principal strain distribution along the Prop top for the ignition pressurization analysis

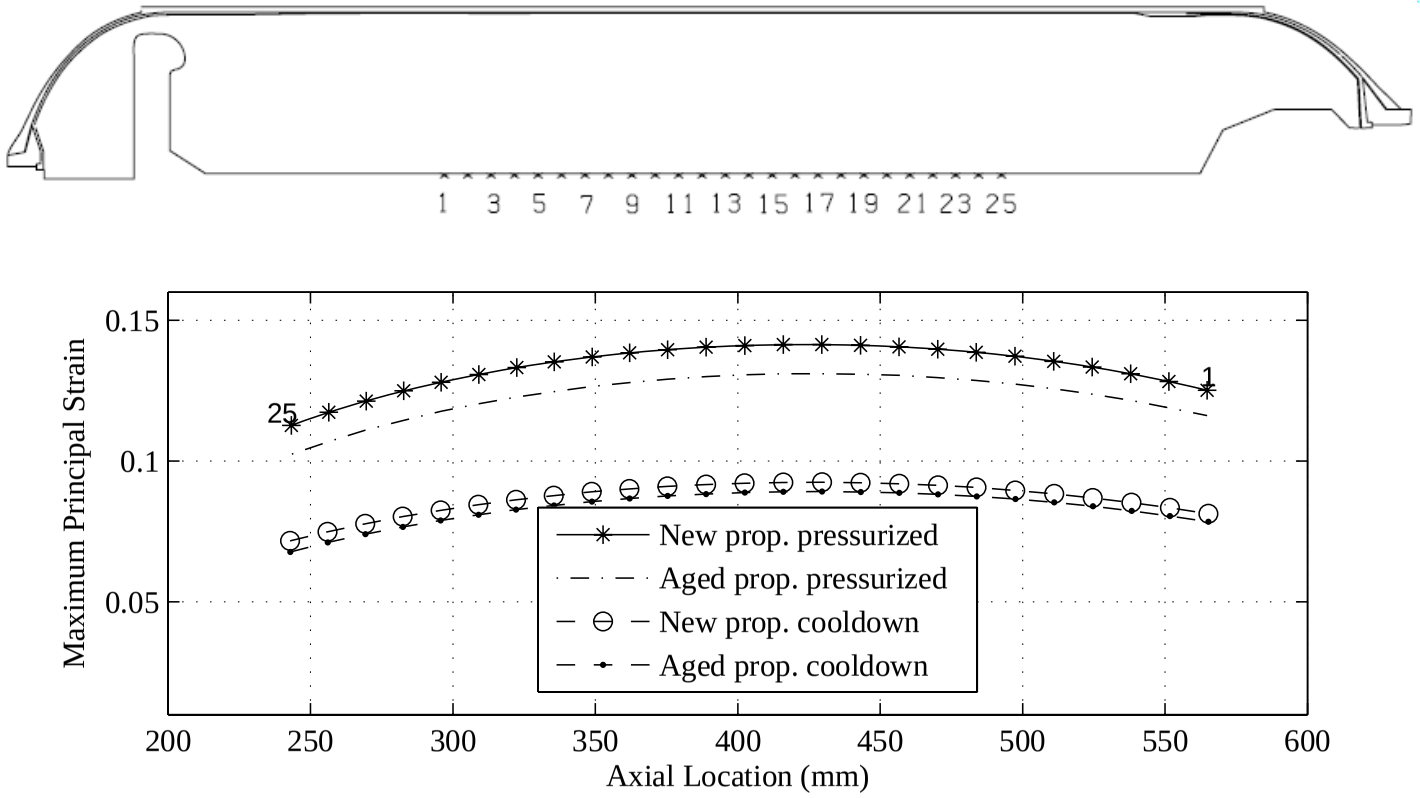

Figure 3.10. Maximum principal strain distribution along the Bore x for the ignition pressurization analysis

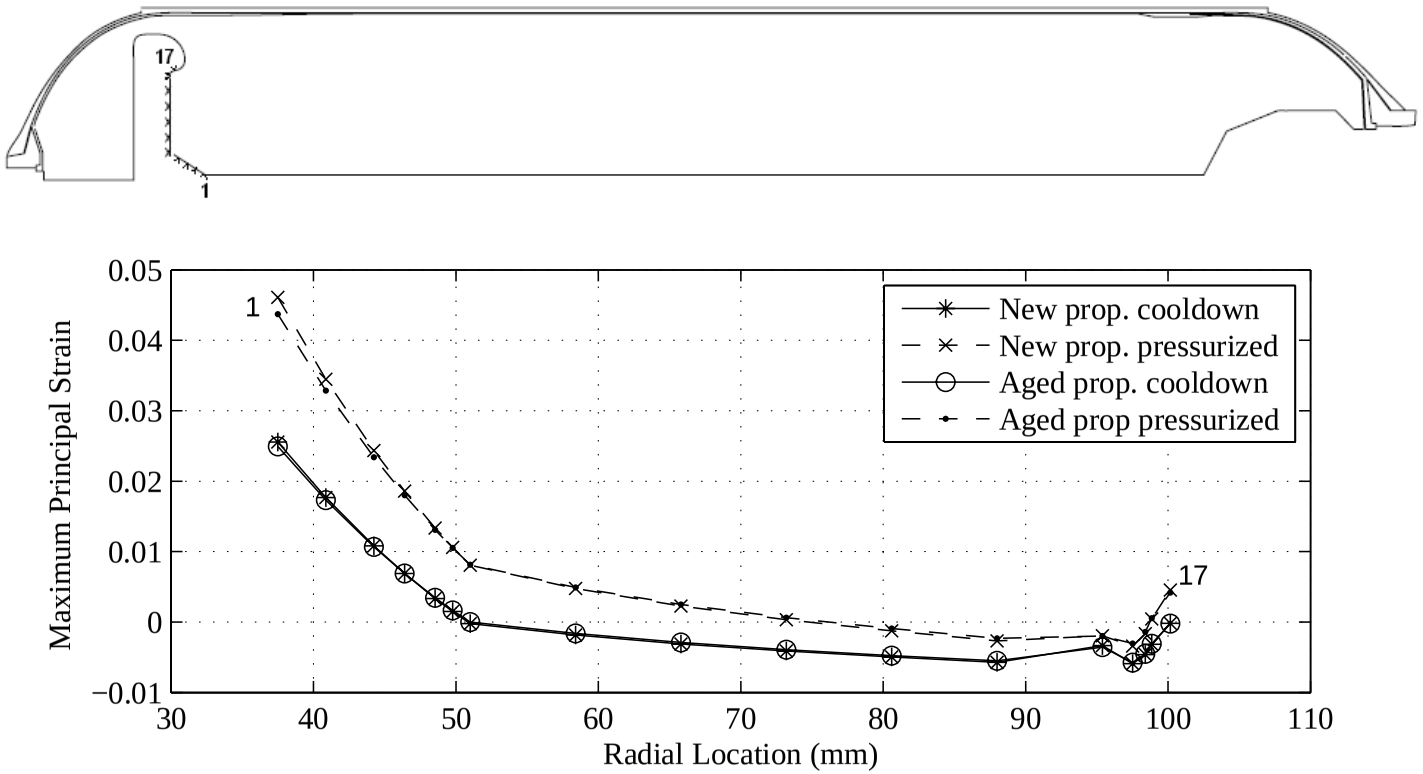

Figure 3.11. Maximum principal strain distribution along the Slot b for the ignition pressurization analysis

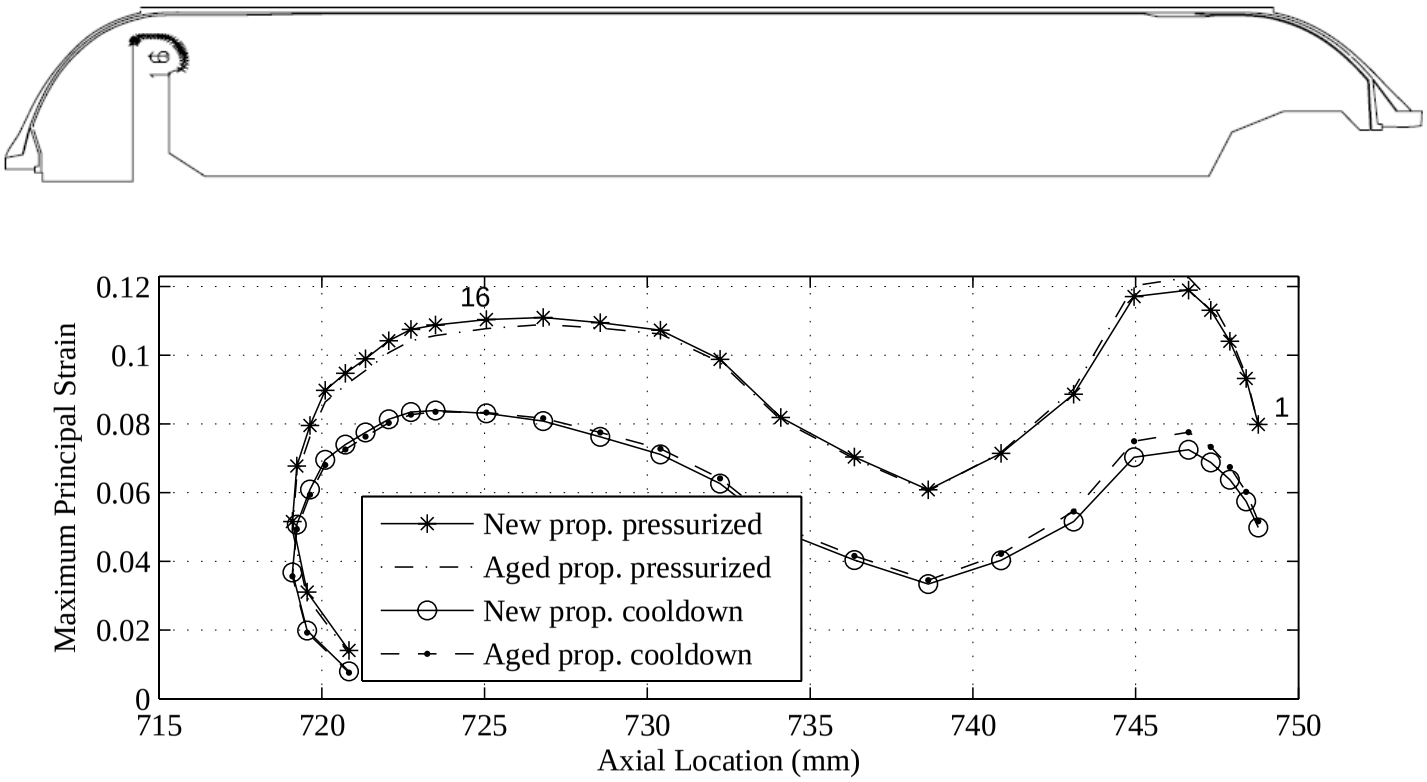

Figure 3.12. Maximum principal strain distribution along the Slot x for the ignition pressurization analysis

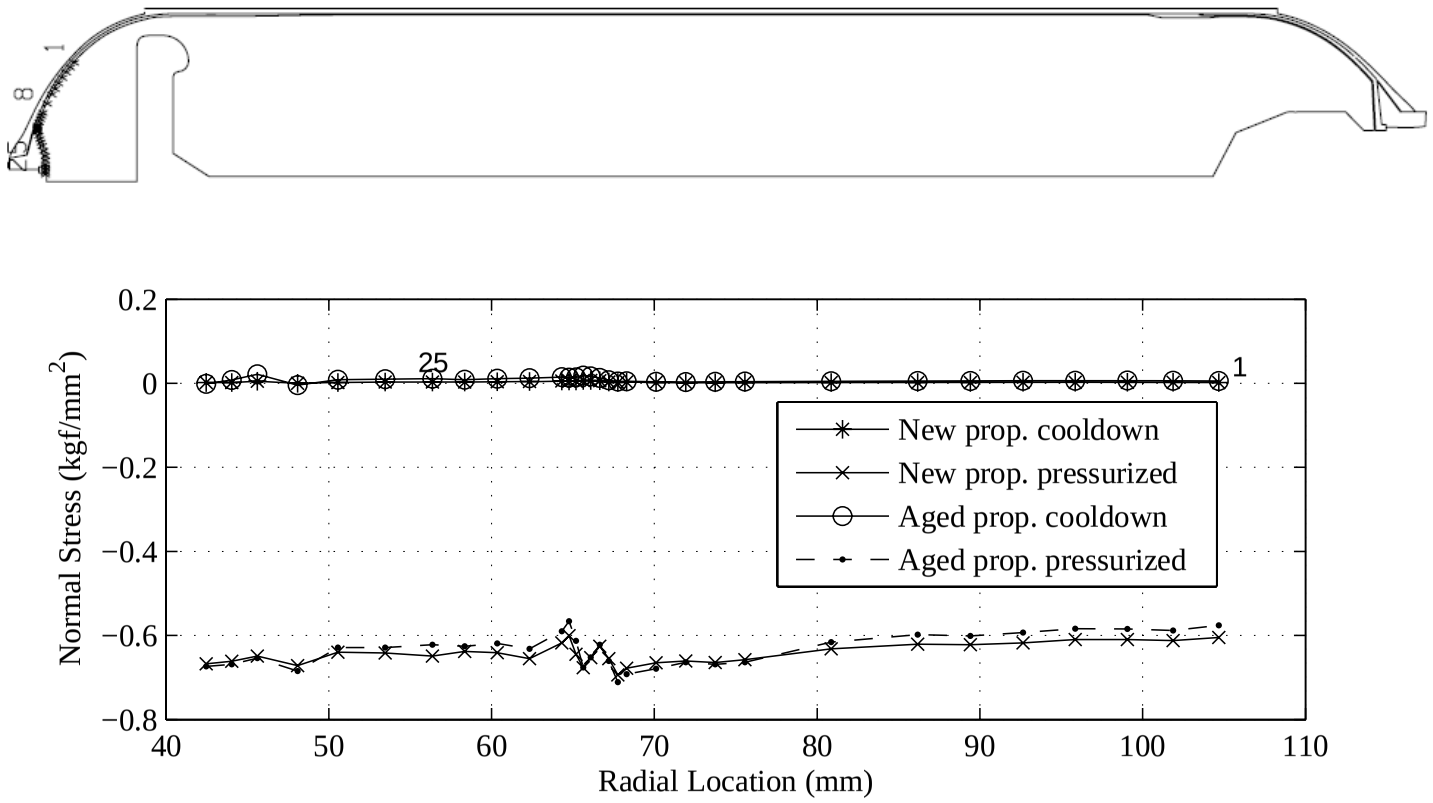

Figure 3.13. Normal stress distribution along the Bond h for the ignition pressurization analysis

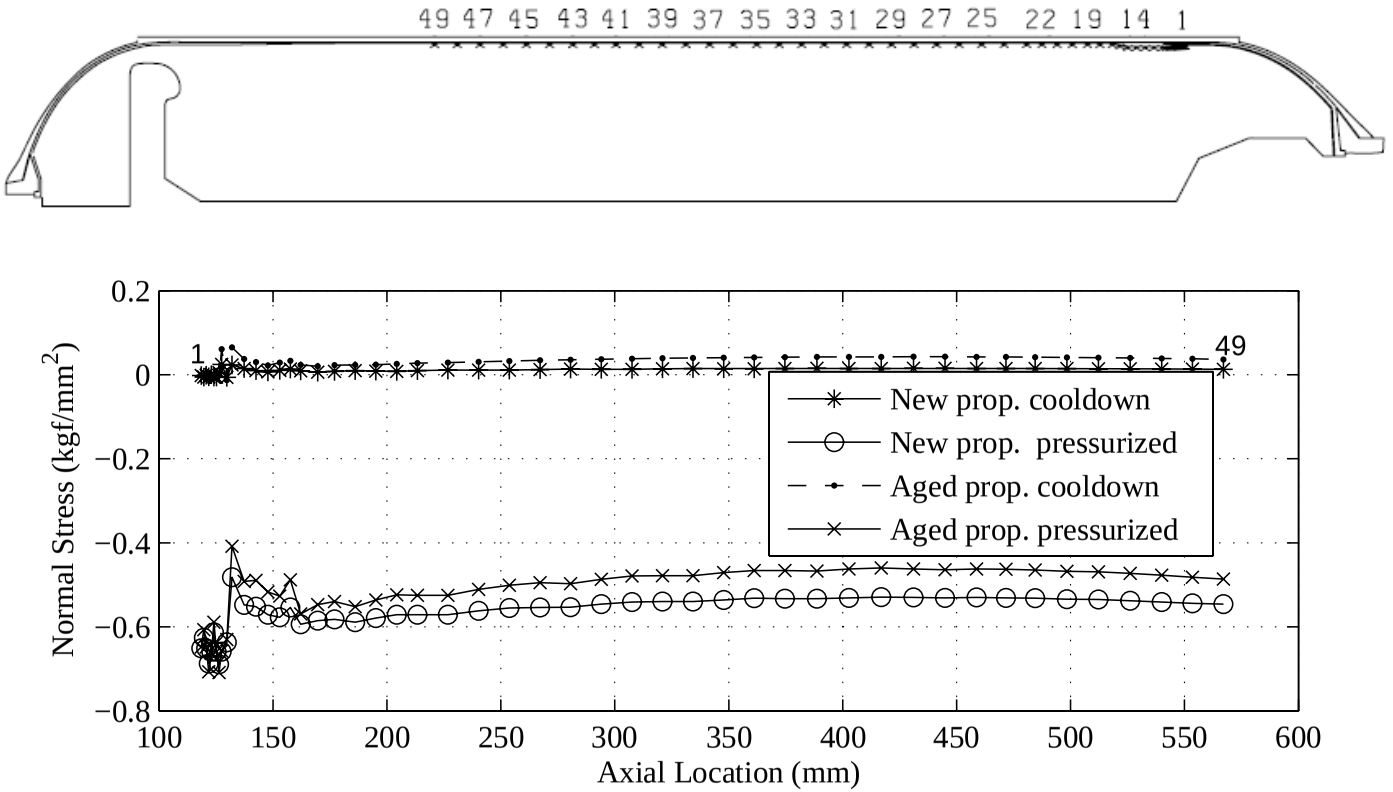

Figure 3.14. Normal stress distribution along the Bond x for the ignition pressurization analysis

3.2.2. Thermal Cycling Analysis

Thermal cycling loading represents possible worst case conditions during the transmission of the rocket motor from one place to another. The thermal cycling profile considered in this study is shown in Figure 3.15. Temperature changes during a cycle are represented with two exponential functions as

$$\begin{aligned} T_{cooldown} &= -32 + 82\exp\left(-Day/0.83\right) \\ T_{warmup} &= 50 - 82\exp\left(-Day/0.83\right) \end{aligned} \tag{3.2}$$

where $T_{cooldown}$ represents cooling and T_{warmup} represents warming within one cycle. Three cycles are analyzed. $50°C$ is defined as the starting temperature in a step for the cycling analysis. Fixed increment is used for the analysis.

Step for thermal cycling analysis is taken as

- *Cooldown & Warmup:* 2400 increments to 2592000 seconds

Figures 3.16 to 3.21 show distributions in critical regions (Table 3.1) of rocket motor after each thermal cycle. Maximum principal strain and bond stress values and their locations are given in Table 3.5 and 3.6 for new and aged propellants, respectively.

Maximum principal strain, ε, is critical for prop top, bore x, slot b, and slot x regions, whereas normal stress, σ, is critical for bond h and bond x regions. Table 3.7 compares calculated values for new and aged propellants. Differences, D, between new and aged propellant are also indicated in Table 3.7. Figures 3.16 to 3.21 state that responses of the critical regions at 432000, 1296000, and 2160000 seconds overlaps for both new and aged materials.

Maximum principal strains for the new propellant are higher than those for the aged propellant. This is expected, since the material response shown in Figure 2.7 states that aged model has a stiffer response than the new one, therefore strain values obtained

from the new model will be greater than those obtained from the aged one. Maximum normal stresses for new model are lower than those for the aged one. Stiffened response of the propellant with aging, as shown in Figure 2.7, explains this result.

Maximum principal strain of 7.95×10^{-2} is obtained at the middle surface of the propellant grain at the end of each cooldown (Figure 3.17). Whereas, maximum normal stress of $5.70\times10^{-2}kg/mm^2$ is calculated at the tip of the free flap at the end of each cooldown (Figure 3.21).

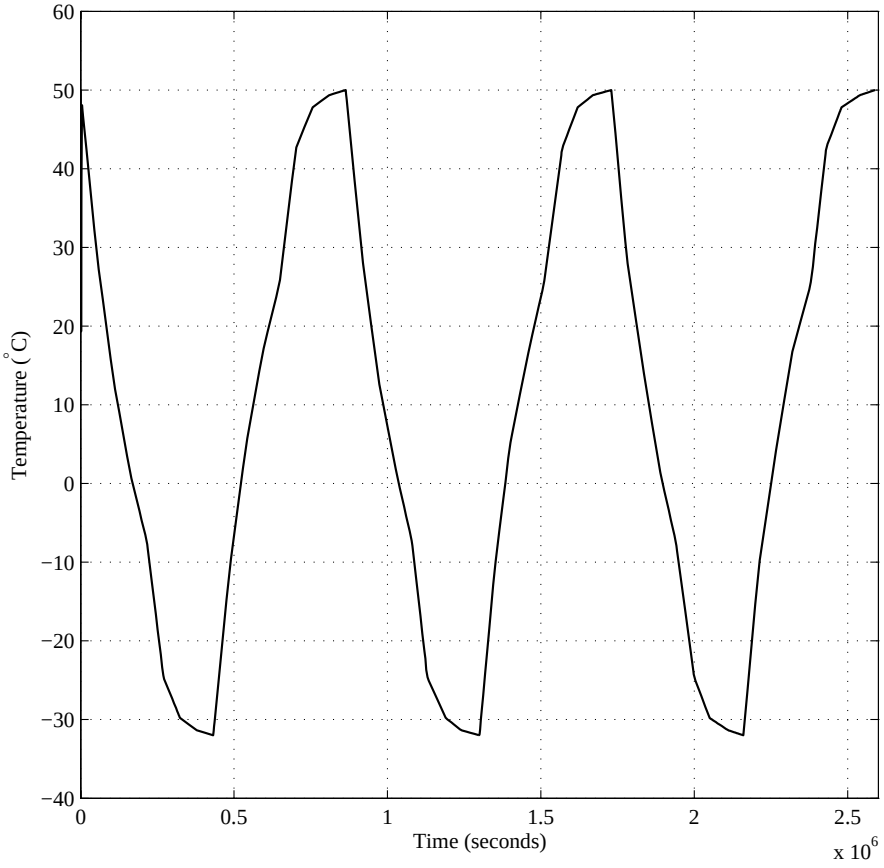

Figure 3.15. Propellant temperature history for thermal cycling

Table 3.5. Maximum principal strains and normal stresses for new propellant and their locations for thermal cycling analysis

Location	Step	Element(s)	Node	Hoop Strain	Bond Stress
					kg/mm^2
Prop top	1st cycle	923	3150	2.055×10^{-2}	-
	2nd cycle	923	3150	2.054×10^{-2}	-
	3d cycle	923	3150	2.055×10^{-2}	-
Bore x	1st cycle	712, 840	2269	8.25×10^{-2}	-
	2nd cycle	712, 840	2269	8.24×10^{-2}	-
	3d cycle	712, 840	2269	8.25×10^{-2}	-
Slot b	1st cycle	371, 372, 642	1277	2.26×10^{-2}	-
	2nd cycle	371, 372, 642	1277	2.26×10^{-2}	-
	3d cycle	371, 372, 642	1277	2.26×10^{-2}	-
Slot x	1st cycle	1125, 1292	3290	7.52×10^{-2}	-
	2nd cycle	1125, 1292	3290	7.51×10^{-2}	-
	3d cycle	1125, 1292	3290	7.52×10^{-2}	-
Bond h	1st cycle	1236, 151	3772	-	6.30×10^{-3}
	2nd cycle	1236, 151	3772	-	6.30×10^{-3}
	3d cycle	1236, 151	3772	-	6.30×10^{-3}
Bond x	1st cycle	526, 322	3900	-	2.28×10^{-2}
	2nd cycle	526, 322	3900	-	2.28×10^{-2}
	3d cycle	526, 322	3900	-	2.28×10^{-2}

Table 3.6. Maximum principal strains and normal stresses for aged propellant and their locations for thermal cycling analysis

Location	Step	Element(s)	Node	Hoop Strain	Bond Stress
					kg/mm^2
Prop top	1st cycle	923	3150	2.045×10^{-2}	-
	2nd cycle	923	3150	2.043×10^{-2}	-
	3d cycle	923	3150	2.045×10^{-2}	-
Bore x	1st cycle	712, 840	2269	7.95×10^{-2}	-
	2nd cycle	712, 840	2269	7.94×10^{-2}	-
	3d cycle	712, 840	2269	7.95×10^{-2}	-
Slot b	1st cycle	371, 372, 642	1277	2.20×10^{-2}	-
	2nd cycle	371, 372, 642	1277	2.20×10^{-2}	-
	3d cycle	371, 372, 642	1277	2.20×10^{-2}	-
Slot x	1st cycle	1125, 1292	3290	7.47×10^{-2}	-
	2nd cycle	1125, 1292	3290	7.46×10^{-2}	-
	3d cycle	1125, 1292	3290	7.47×10^{-2}	-
Bond h	1st cycle	1236, 151	3772	-	1.63×10^{-2}
	2nd cycle	1236, 151	3772	-	1.63×10^{-2}
	3d cycle	1236, 151	3772	-	1.63×10^{-2}
Bond x	1st cycle	526, 489	1215	-	5.70×10^{-2}
	2nd cycle	526, 489	1215	-	5.70×10^{-2}
	3d cycle	526, 489	1215	-	5.70×10^{-2}

Table 3.7. Maximum principal strains and maximum normal stresses after 300,900,and 1500 increments for cycling analysis

Increment:	300 (432000sec)			600 (1296000sec)			1500 (2160000sec)		
Model:	New	Aged	D	New	Aged	D	New	Aged	D
Prop top, ε	2.055×10^{-2}	2.045×10^{-2}	0.48%	2.054×10^{-2}	2.043×10^{-2}	0.48%	2.055×10^{-2}	2.045×10^{-2}	0.48%
Bore x, ε	8.25×10^{-2}	7.95×10^{-2}	3.63%	8.24×10^{-2}	7.94×10^{-2}	3.63%	8.25×10^{-2}	7.95×10^{-2}	3.63%
Slot b, ε	2.26×10^{-2}	2.20×10^{-2}	2.65%	2.26×10^{-2}	2.20×10^{-2}	2.65%	2.26×10^{-2}	2.20×10^{-2}	2.65%
Slot x, ε	7.52×10^{-2}	7.47×10^{-2}	0.66%	7.52×10^{-2}	7.46×10^{-2}	0.66%	7.52×10^{-2}	7.47×10^{-2}	0.66%
Bond h, σ	6.3×10^{-3}	1.63×10^{-2}	158%	6.3×10^{-3}	1.63×10^{-2}	158%	6.3×10^{-3}	1.63×10^{-2}	158%
Bond x, σ	2.28×10^{-2}	5.70×10^{-2}	150%	2.28×10^{-2}	5.70×10^{-2}	150%	2.28×10^{-2}	5.70×10^{-2}	150%

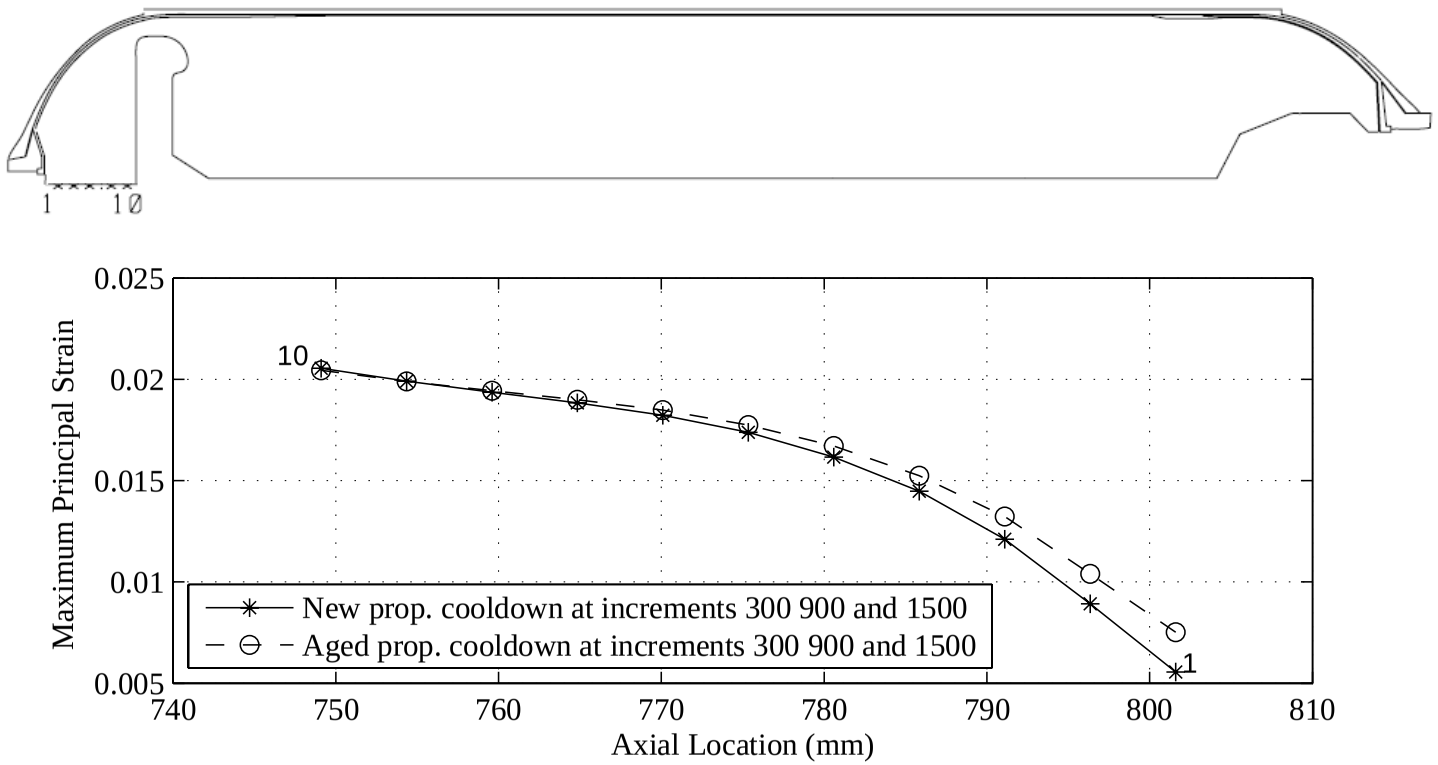

Figure 3.16. Maximum principal strain distribution along the Prop top for the thermal cycling analysis

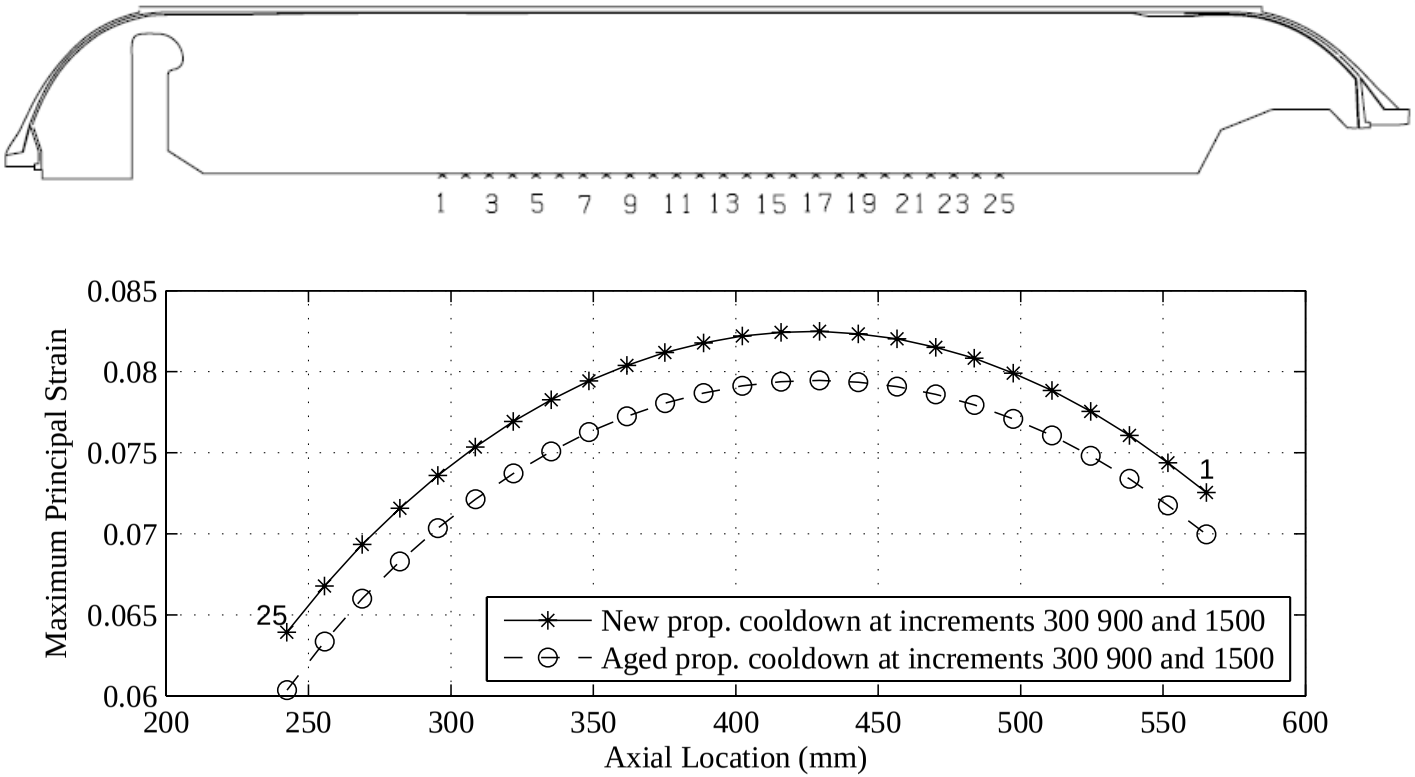

Figure 3.17. Maximum principal strain distribution along the Bore x for the thermal cycling analysis

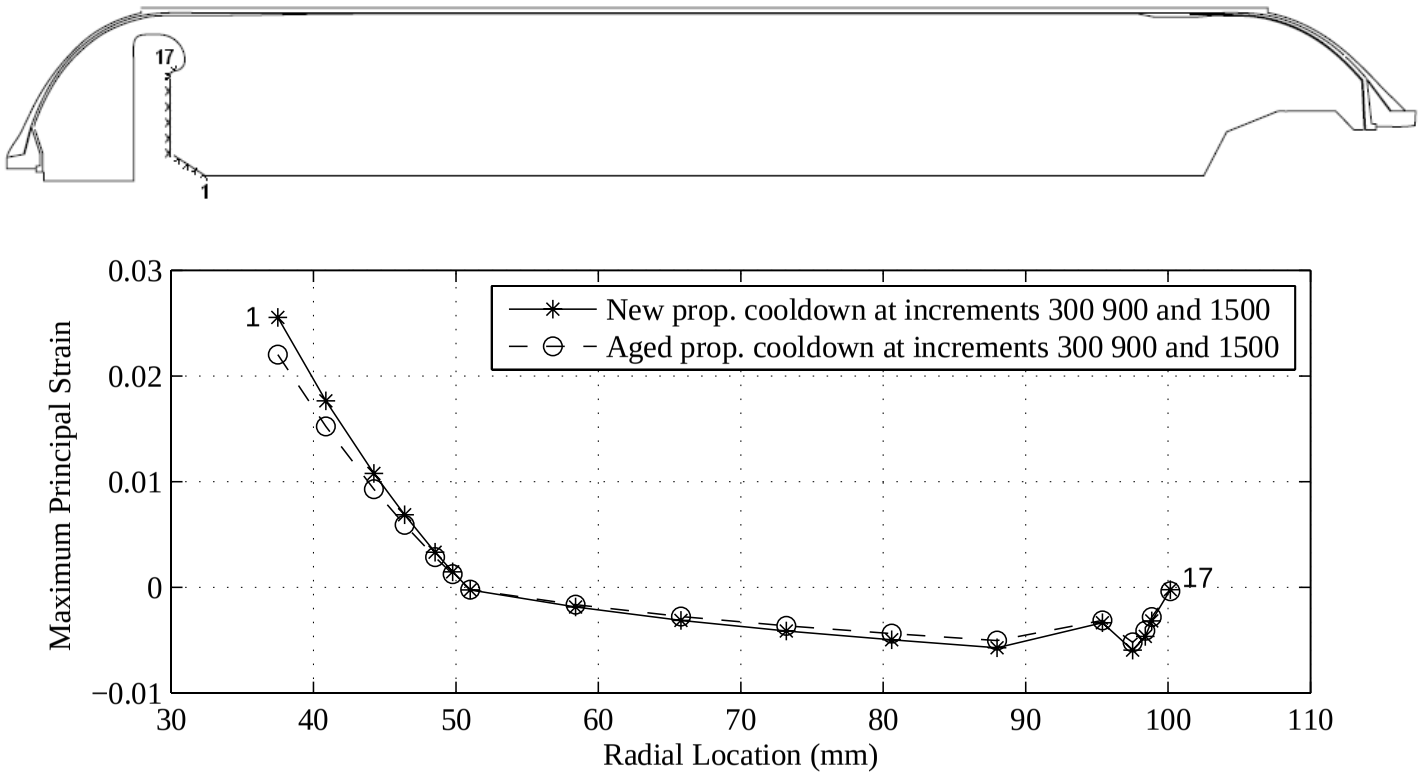

Figure 3.18. Maximum principal strain distribution along the Slot b for the thermal cycling analysis

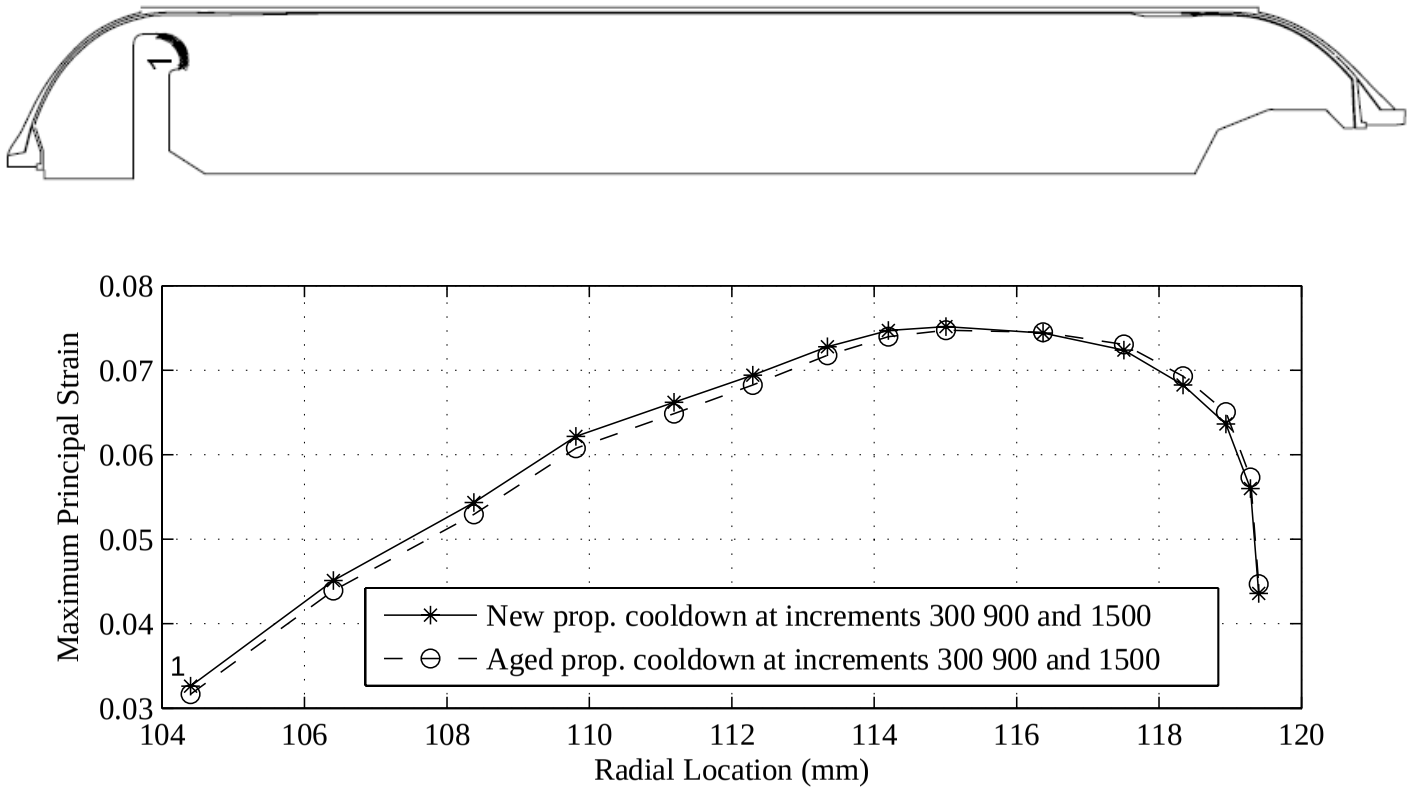

Figure 3.19. Maximum principal strain distribution along the Slot x for the thermal cycling analysis

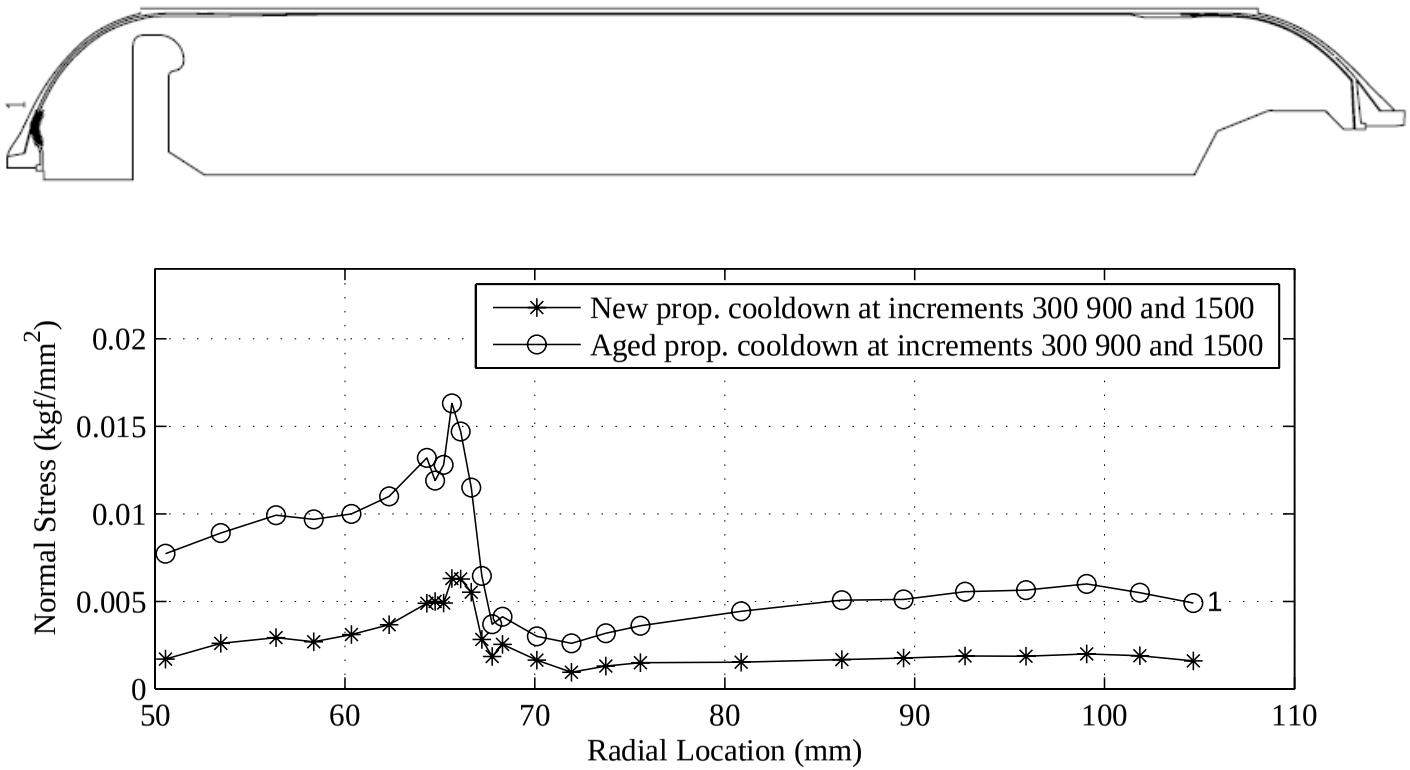

Figure 3.20. Normal stress distribution along the Bond h for the thermal cycling analysis

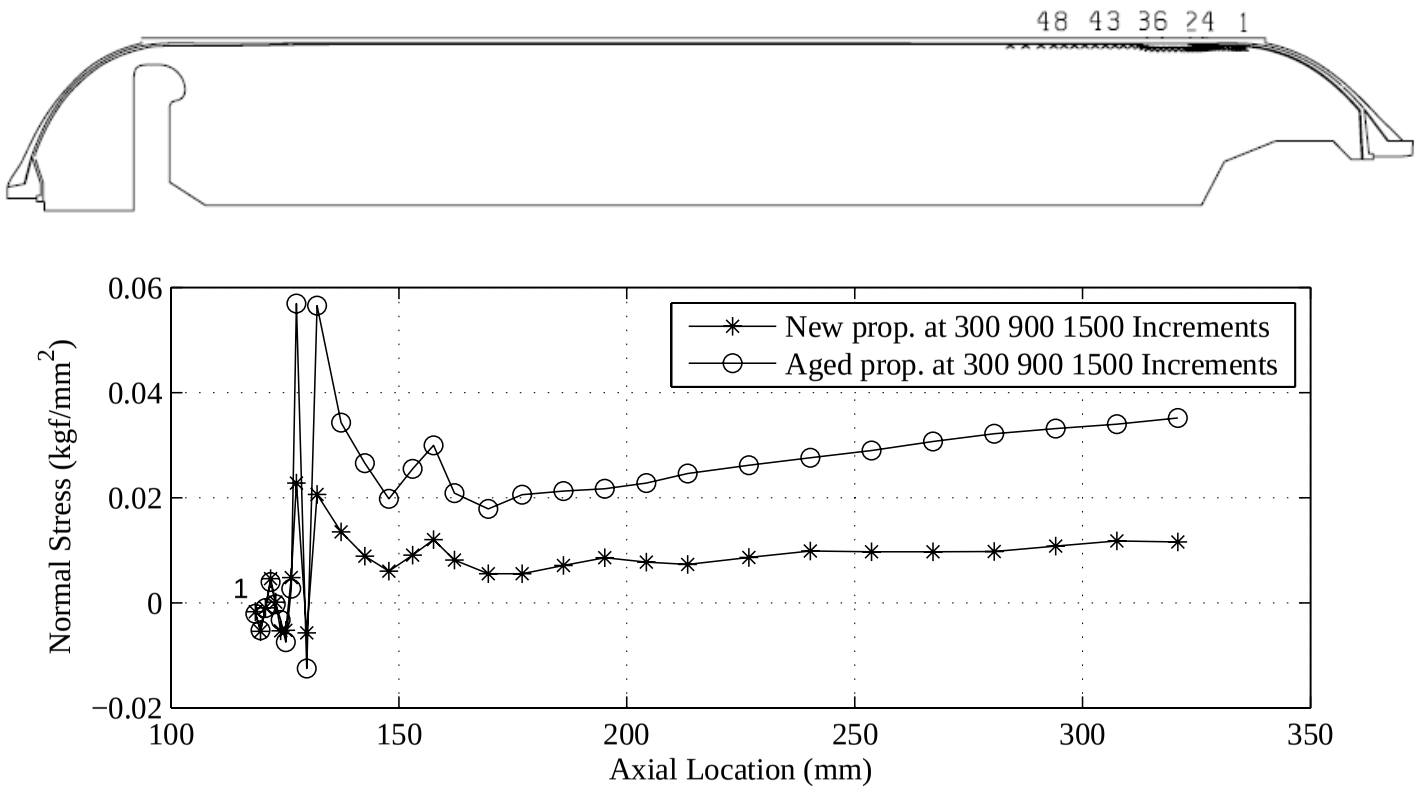

Figure 3.21. Normal stress distribution along the Bond x for the thermal cycling analysis

3.2.3. Thermal Storage Analysis

The temperature profile for storage analysis is constructed based on temperature changes during the year, as well during the day. The worst case scenario for thermal loading is defined as a two step loading, first step is cooling down from $50°C$ to yearly averaged temperature, and second step is again cooling down along the path from average to coldest temperature. Fixed increment is used for the analysis. The resulting temperature loading profile is presented in Figure 3.22.

Step for thermal storage analysis is taken as

- *Cooldown :* 918 increments to 7927200 seconds ($50°C$ to $-10°C$)

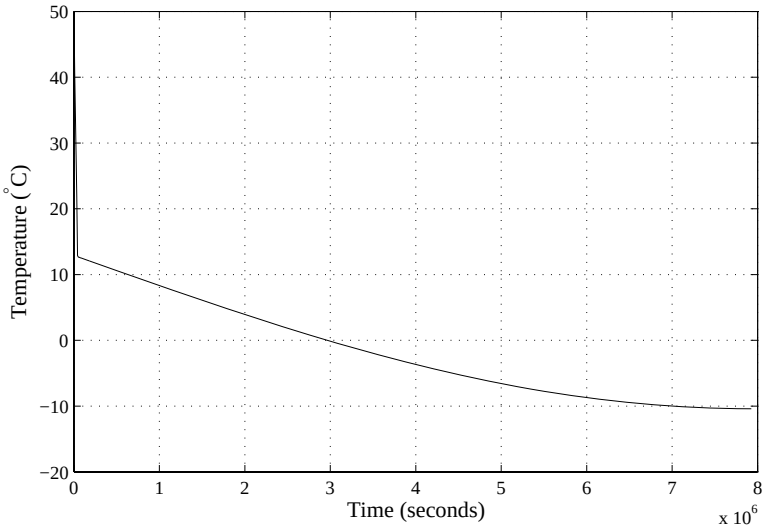

Figure 3.22. Propellant temperature history for thermal storage

Figures 3.23 to 3.28 show results at the end of the thermal storage analysis for regions identified in Table 3.1. Maximum principal strain and bond stress values and their locations are given in Table 3.8 and 3.9 for new and aged propellants, respectively. Table 3.10 compares calculated values for new and aged propellants.

As in the case of other loadings, Table 3.10 shows that maximum principal strain occurred in the new propellant model are greater than those of aged one. This is

expected, since the material response shown in Figure 2.7 states that aged model has a stiffer response than the new one, therefore strain values obtained from the new model will be greater than those obtained from the aged one. Maximum normal stresses for new model are lower than those for the aged one. Since aged material response in Figure 2.7 is stiffer than that for the new one, this result is reasonable.

Maximum principal strain of 5.90×10^{-2} is obtained at the middle surface of the propellant grain at the end of cooldown (Figure 3.24). Whereas, maximum normal stress $4.14\times10^{-2} kg/mm^2$ is calculated at the tip of the free flap for cooldown process (Figure 3.28).

Table 3.8. Maximum principal strains and normal stresses for new propellant and their locations for thermal storage analysis

Location	Element(s)	Node	Hoop Strain	Bond Stress
				kg/mm^2
Prop top x	923	3150	1.52×10^{-2}	-
Bore x	712, 840	2269	6.08×10^{-2}	-
Slot b	371, 372, 642	1277	1.63×10^{-2}	-
Slot x	1125, 1292	3290	5.59×10^{-2}	-
Bond h	1236, 151	3772	-	4.40×10^{-3}
Bond x	322, 526	3900	-	1.17×10^{-2}

Table 3.9. Maximum principal strains and normal stresses for aged propellant and their locations for thermal storage analysis

Location	Element(s)	Node	Hoop Strain	Bond Stress
				kg/mm^2
Prop top x	923	3150	1.51×10^{-2}	-
Bore x	712, 840	2269	5.90×10^{-2}	-
Slot b	371, 372, 642	1277	1.60×10^{-2}	-
Slot x	1125, 1292	3290	5.54×10^{-2}	-
Bond h	1236, 151	3772	-	4.40×10^{-3}
Bond x	322, 526	3900	-	9.90×10^{-3}

Table 3.10. Maximum principal strains and maximum normal stresses at last step for thermal storage analysis

Increment:	7927200 sec		
Model:	New	Aged	D
Prop top, ε	1.52×10^{-2}	1.51×10^{-2}	0.66%
Bore x, ε	6.08×10^{-2}	5.90×10^{-2}	2.96%
Slot b, ε	1.63×10^{-2}	1.60×10^{-2}	1.84%
Slot x, ε	55.89×10^{-3}	55.43×10^{-3}	0.83%
Bond h, σ	4.40×10^{-3}	9.90×10^{-3}	55%
Bond x, σ	1.77×10^{-2}	4.14×10^{-2}	57%

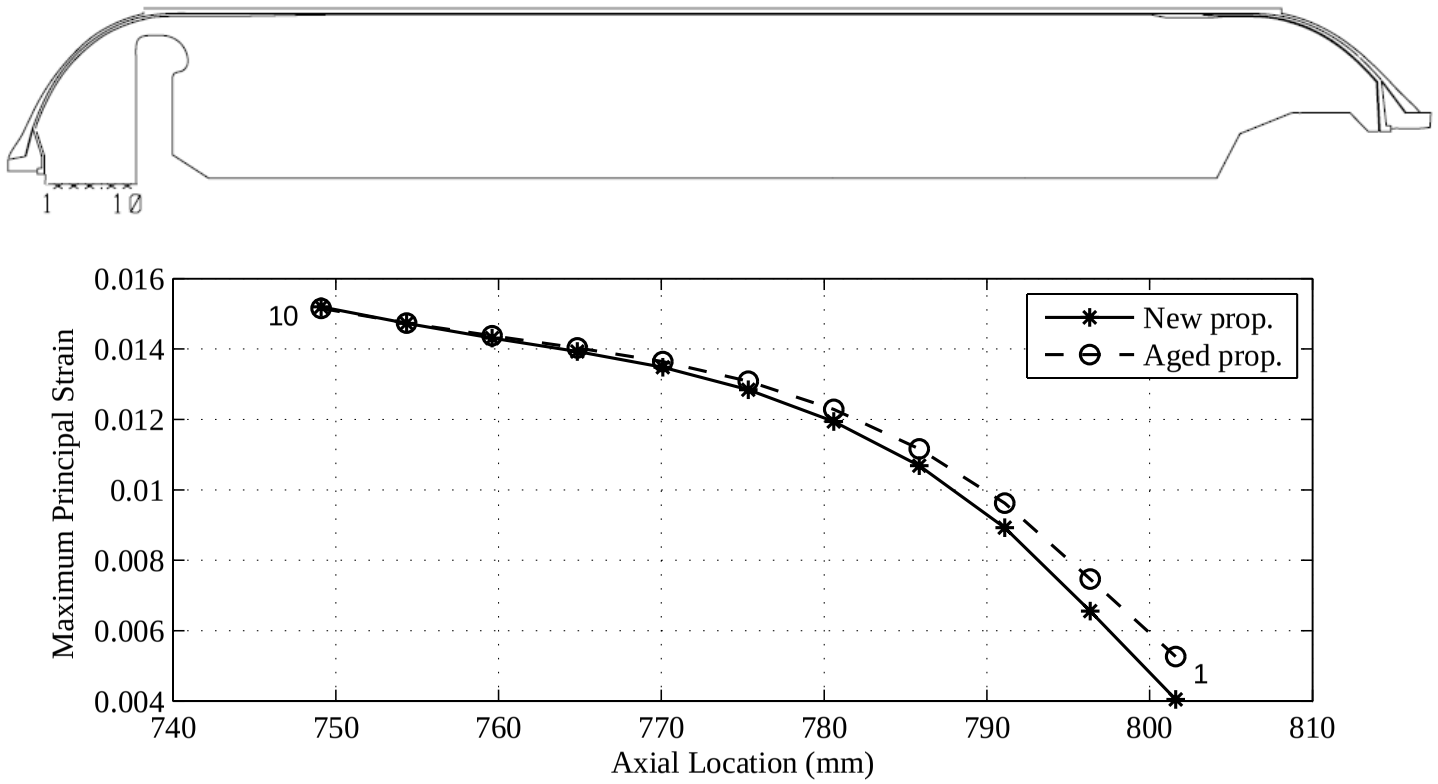

Figure 3.23. Maximum principal strain distribution along the Prop top for the thermal storage analysis

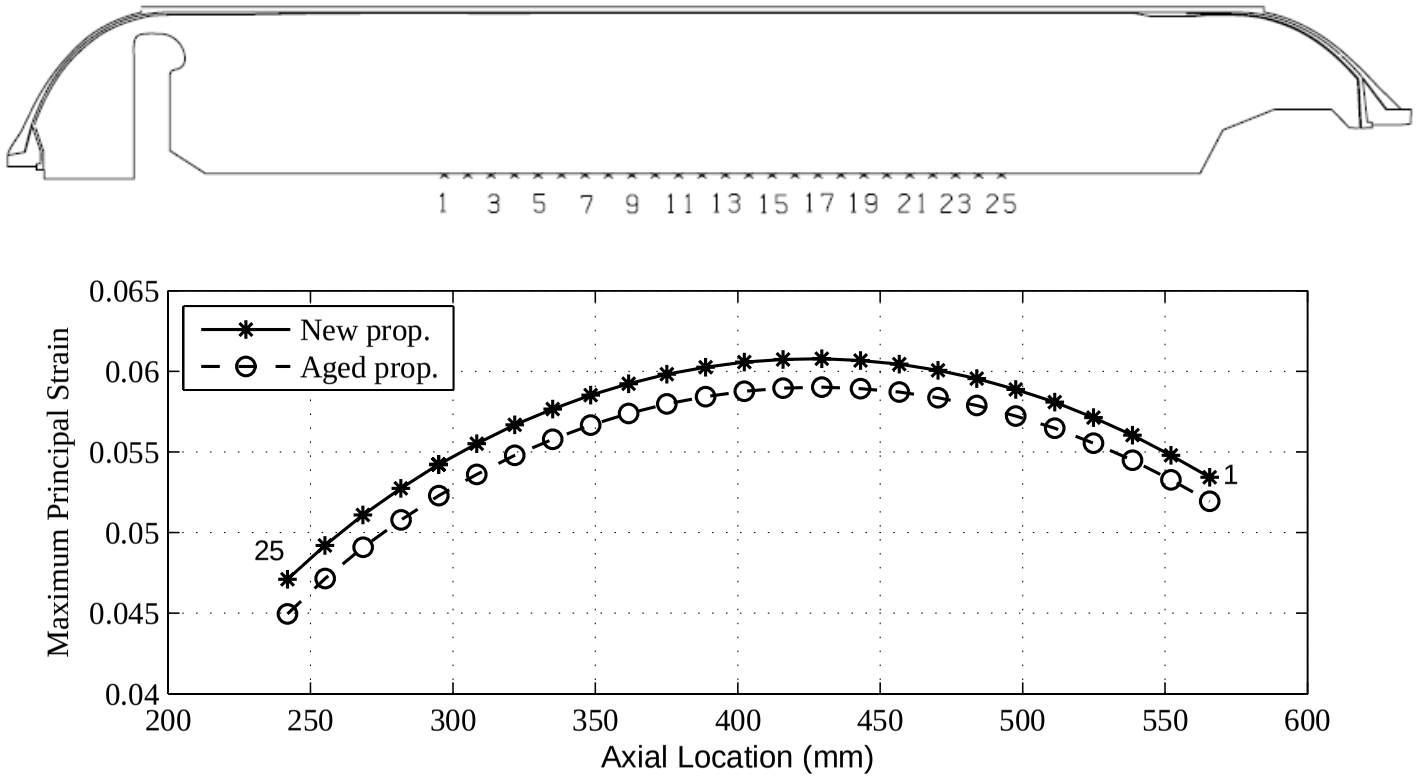

Figure 3.24. Maximum principal strain distribution along the Bore x for the thermal storage analysis

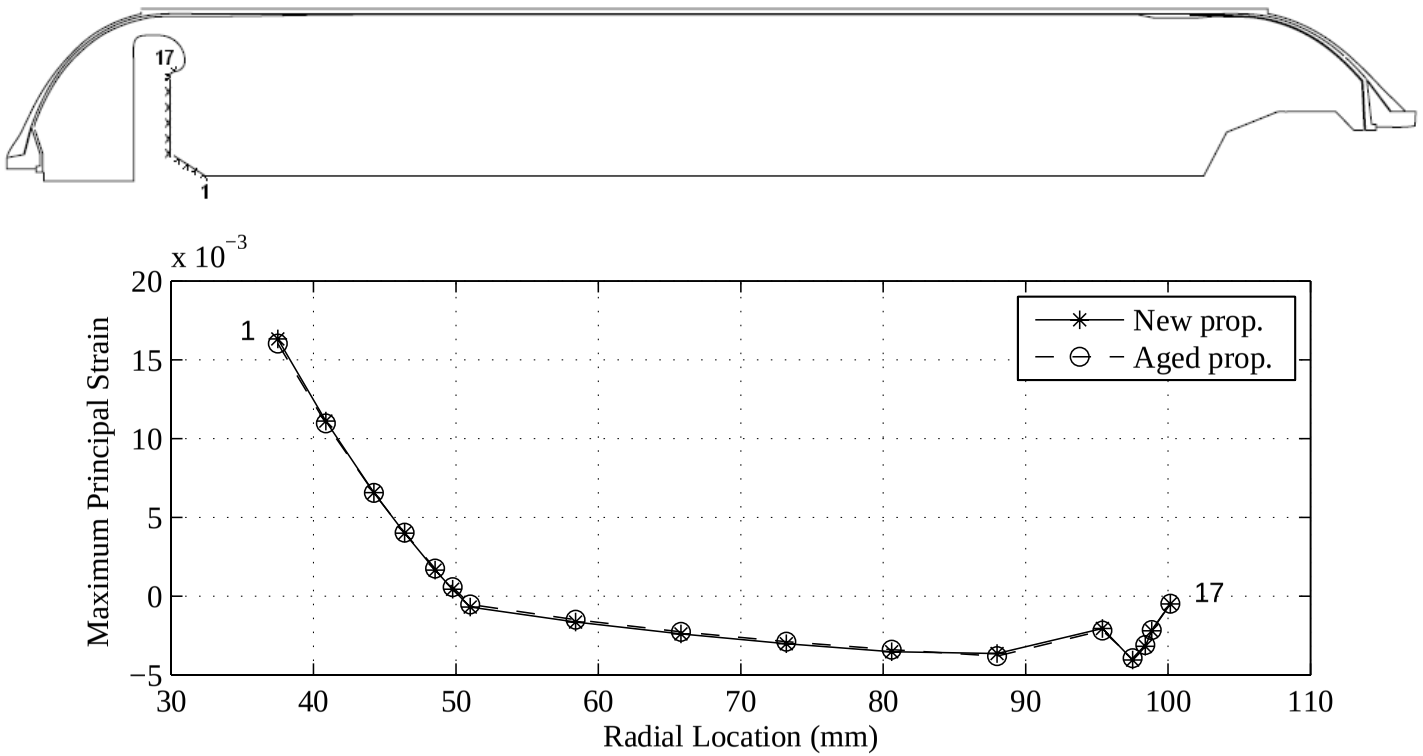

Figure 3.25. Maximum principal strain distribution along the Slot b for the thermal storage analysis

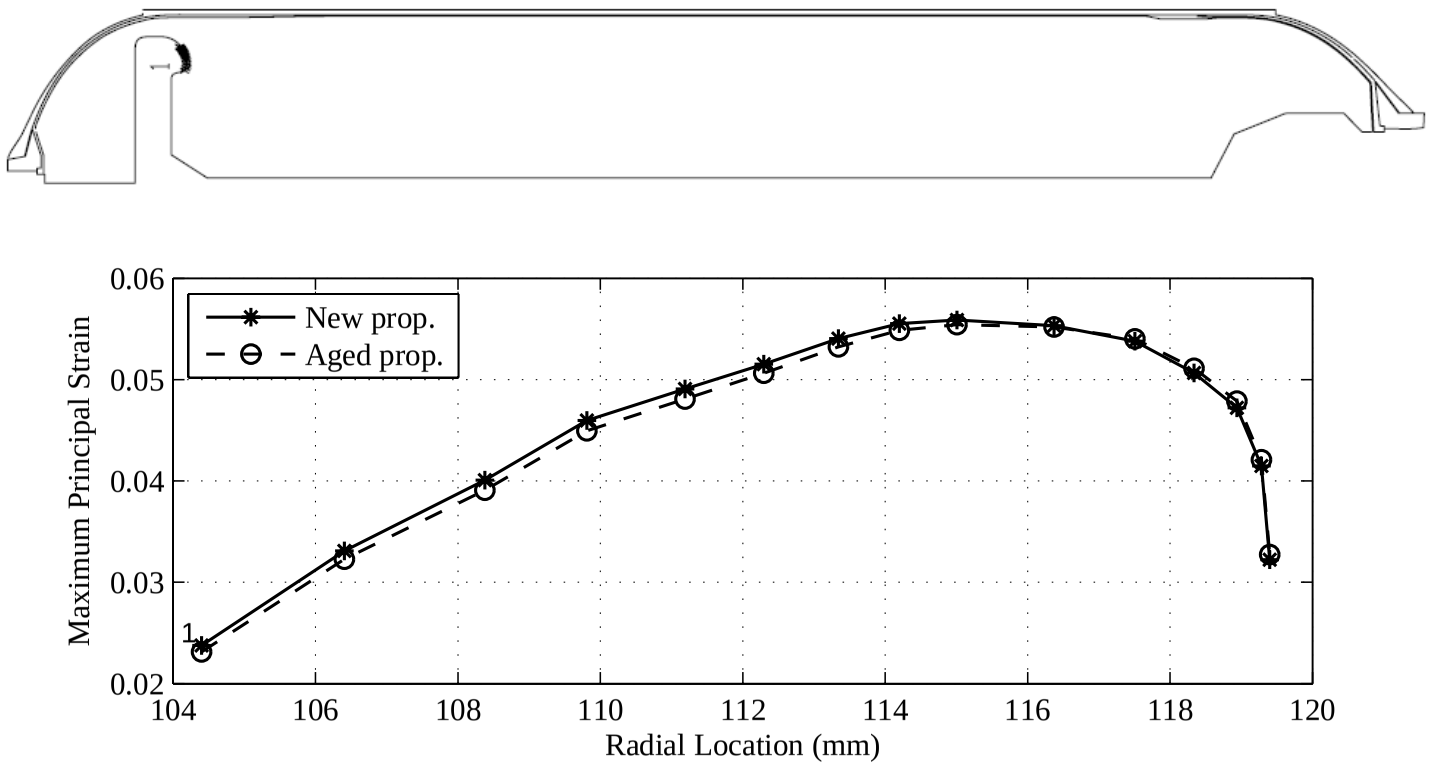

Figure 3.26. Maximum principal strain distribution along the Slot x for the thermal storage analysis

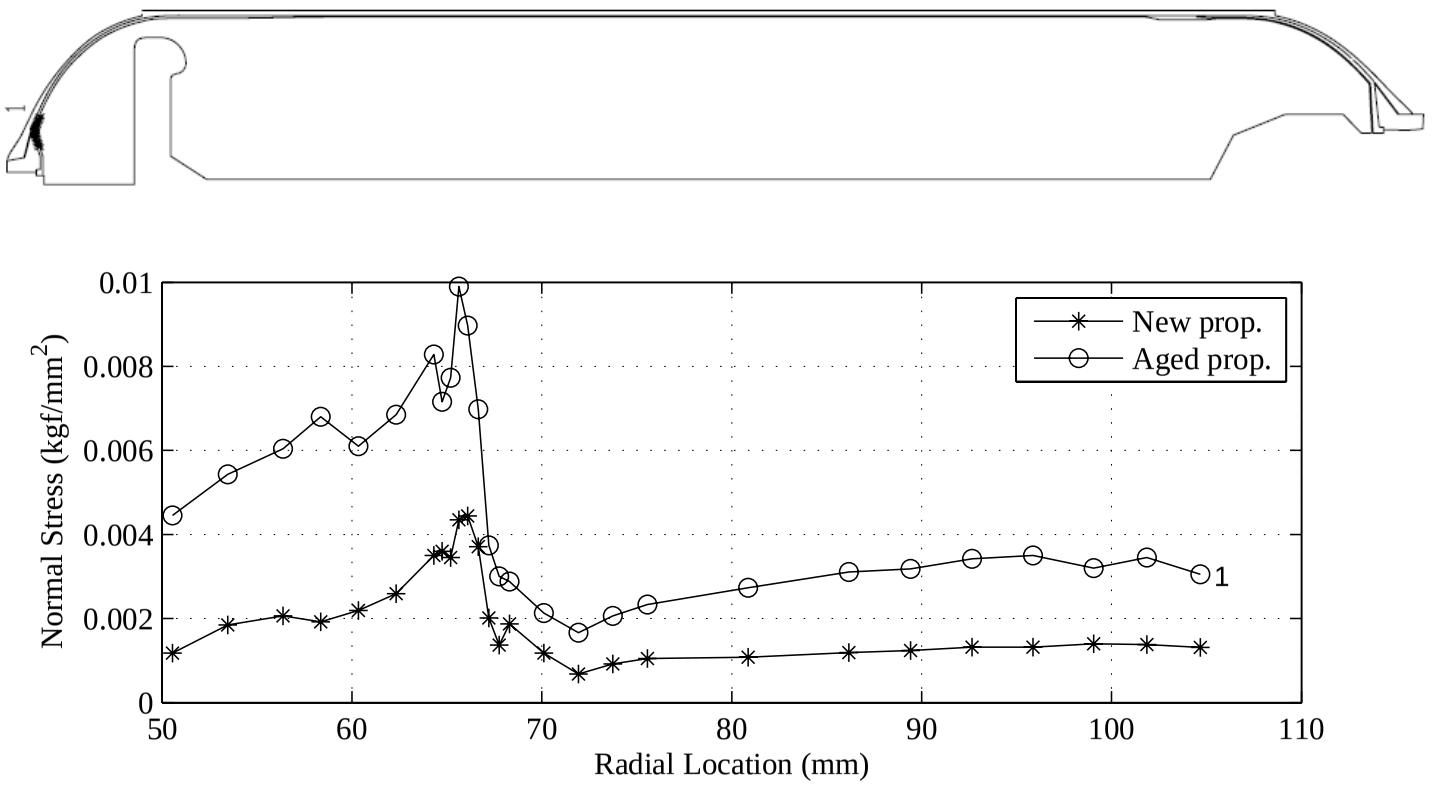

Figure 3.27. Normal stress distribution along the Bond h for the thermal storage analysis

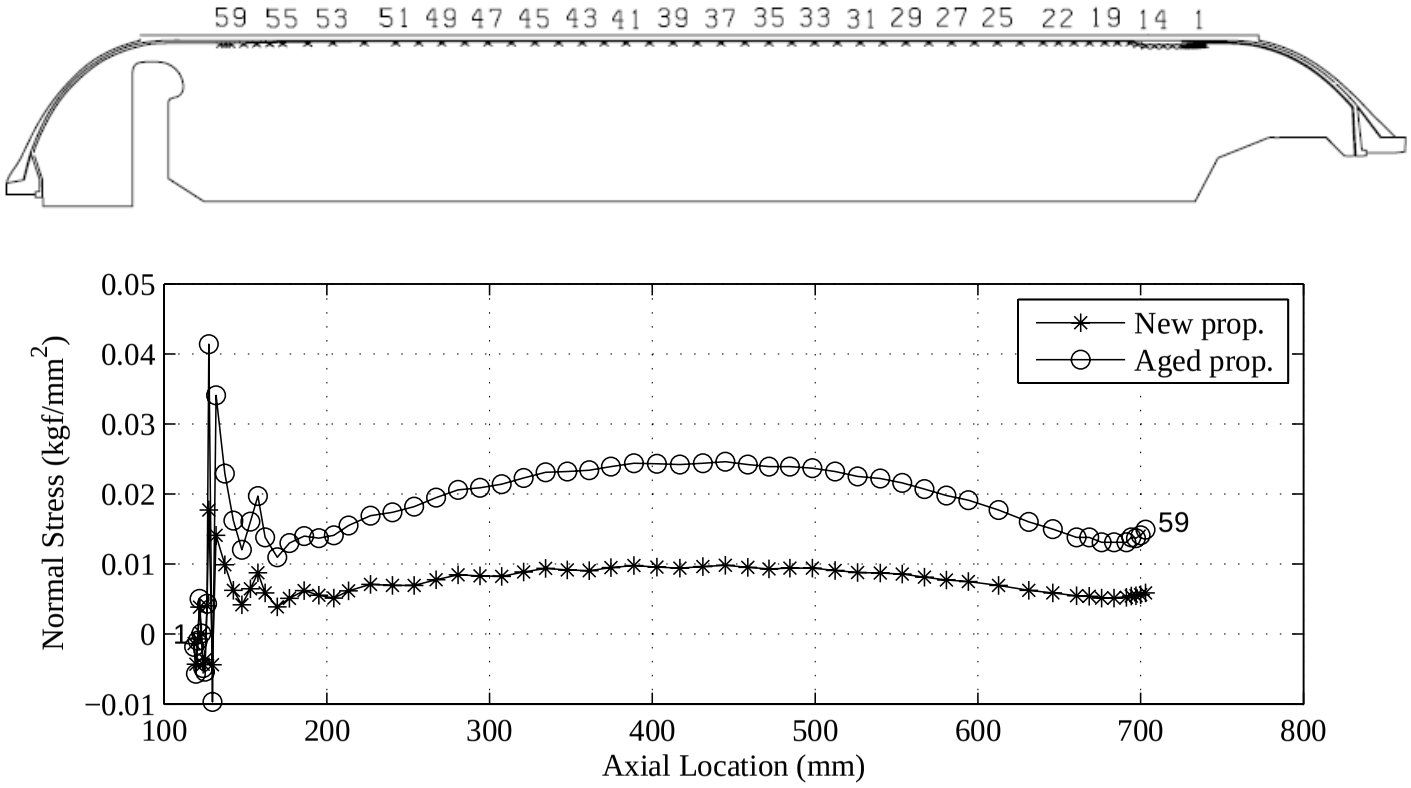

Figure 3.28. Normal stress distribution along the Bond x for the thermal storage analysis

3.3. Summary of Finite Element Analyses

Maximum principal strain and maximum normal stress values for each loading are summarized in Table 3.11 and Table 3.12 for new and aged propellants, respectively.

For the new propellant, maximum hoop strain of 1.39×10^{-1} occurred at the middle surface of the propellant in ignition pressurization analysis. Whereas, maximum normal stress of 2.43×10^{-2} is calculated between the liner and the insulator at the tip of the free flap in ignition pressurization analysis. The contour plot of solid propellant for the ignition pressurization analysis is illustrated at Figure B.1 in Appendix B.

Table 3.11. Maximum principal strains and maximum normal stresses for new propellant

Type:	Hoop strain			Bond stress, kg/mm^2		
	Step	Region	Value	Step	Region	Value
Pressure	Pressure	Bore x	$\mathbf{1.39\times10^{-1}}$	Cooldown	Bond x	$\mathbf{2.43\times10^{-2}}$
Cycling	Cooldown	Bore x	8.25×10^{-2}	Cooldown	Bond x	2.28×10^{-2}
Storage	Cooldown	Bore x	6.08×10^{-2}	Cooldown	Bond x	1.77×10^{-2}

For the aged propellant, maximum hoop strain of 1.29×10^{-1} occurred at the middle surface of the propellant in ignition pressurization analysis. Whereas, maximum normal stress of 6.50×10^{-2} is calculated between the liner-insulator at the tip of the free flap in ignition pressurization analysis.

From the bond stress point of view, liner-insulator interface at the tip of the free flap is the critical location for all cooldown processes.

Tables 3.11 and 3.12 state that, the maximum principal strain values are close to each other for new and aged propellants. Bond stress values of new and aged propellants, on the other hand, are quite different from each other. Therefore, it is expected that the maximum bond stress will be the critical value, and liner-insulator interface at the tip of free flap will be the critical region when determining the lifetime

Table 3.12. Maximum principal strains and maximum normal stresses for aged propellant

Type:	Hoop strain			Bond stress, kg/mm^2		
	Step	Region	Value	Step	Region	Value
Pressure	Pressure	Bore x	$\mathbf{1.29 \times 10^{-1}}$	Cooldown	Bond x	$\mathbf{6.50 \times 10^{-2}}$
Cycling	Cooldown	Bore x	7.95×10^{-2}	Cooldown	Bond x	5.70×10^{-2}
Storage	Cooldown	Bore x	5.90×10^{-2}	Cooldown	Bond x	4.14×10^{-2}

of solid rocket motor.

4. CONCLUSIONS

The main objective of this thesis was to do structural analysis of a solid propellant rocket motor considering the effect of aging. Finite element models were constructed using nonlinear viscoelastic constitutive models for new and aged propellants. Ignition pressurization, thermal cycling, and thermal storage loadings were analyzed. Maximum principal strain at the surface of the propellant and normal stresses at the interface between the liner and the insulator were evaluated as indicators of cracking in the propellant grain and debonding at the interface. Maximum hoop strain occurred at the middle-surface of the grain for all loadings. Maximum bond stresses were calculated at the tip of the free flap in all cooldown analyses.

The differences between new and aged propellants are small for maximum principal strains, whereas the differences between new and aged propellants are quite large for maximum normal stresses. Therefore, it is likely that maximum bond stress will be the critical value, and liner-insulator interface at the tip of free flap will be the critical region when determining the lifetime of solid rocket motor.

A number of assumptions were made during the study. The nonlinear viscoelastic model used in the study is a non-damaging one, and the predicted response is independent of the pressure level. Analysis results show that strain and stress levels for the loadings considered are in the region where the effect of pressure is not very significant, therefore the assumed constitutive representation is acceptable. As a future study, it would be desirable to include the effect of damage and pressure into the constitutive model. It would be expected that for non-pressurized analysis maximum principal strains obtained from a damaging model would be higher than those predicted in this study. On the other hand, normal stresses would be smaller than those calculated in this study. For the pressurized analysis no significant difference would be expected.

The results obtained in this study can be used to estimate the service life of the rocket motor. For such estimation the strain capability and bond-strength data for

different ages of the solid propellant should be available. The maximum stress and strain values calculated in this study would be compared with the capabilities to determine if a propellant at the considered age could be safely fired. Furthermore, if aging trends could be established on both the response and capabilities, then extrapolation to future times could be done, therefore life of the motor could be estimated. Analyses may be repeated for planned intervals in the future, and estimation could be adjusted accordingly.

APPENDIX A: SECTIONS OF THE ROCKET MOTOR

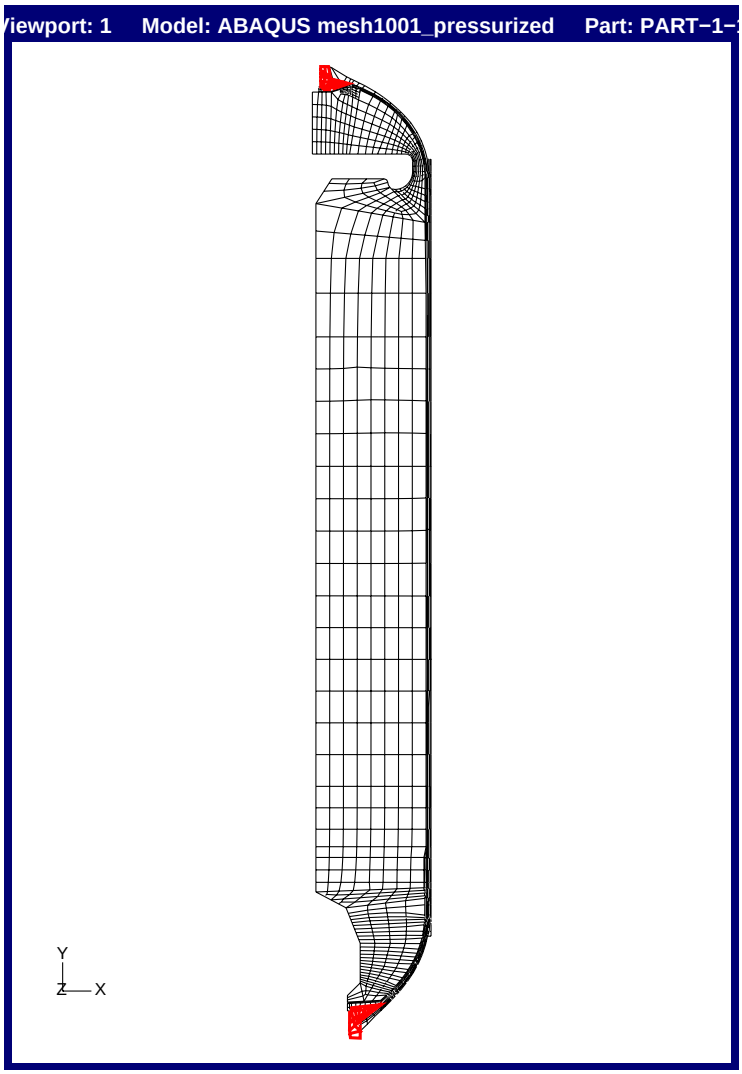

Figure A.1. Aluminium Boss section in ABAQUS CAE

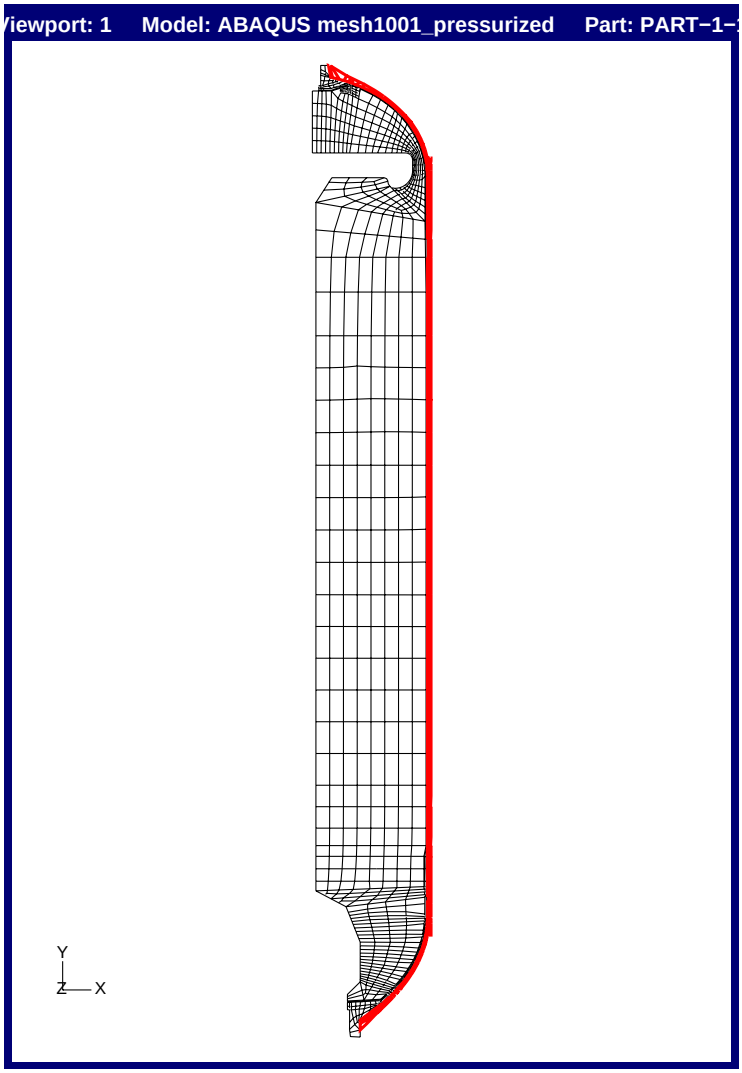

Figure A.2. Case section in ABAQUS CAE

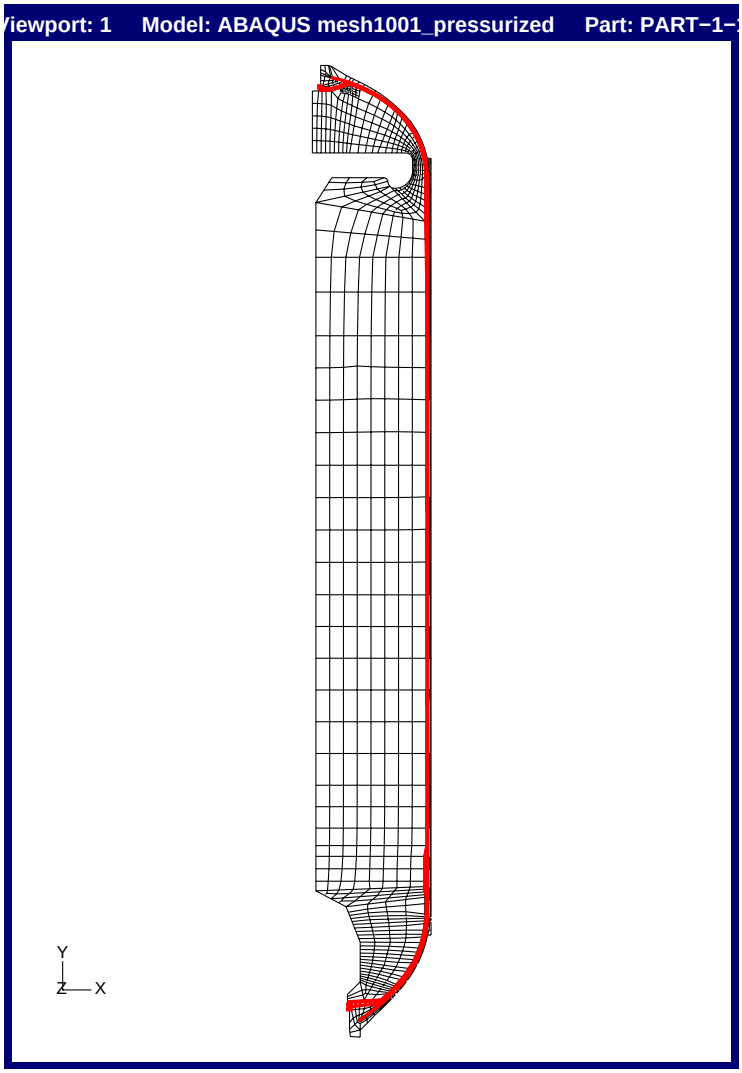

Figure A.3. EPDM section in ABAQUS CAE

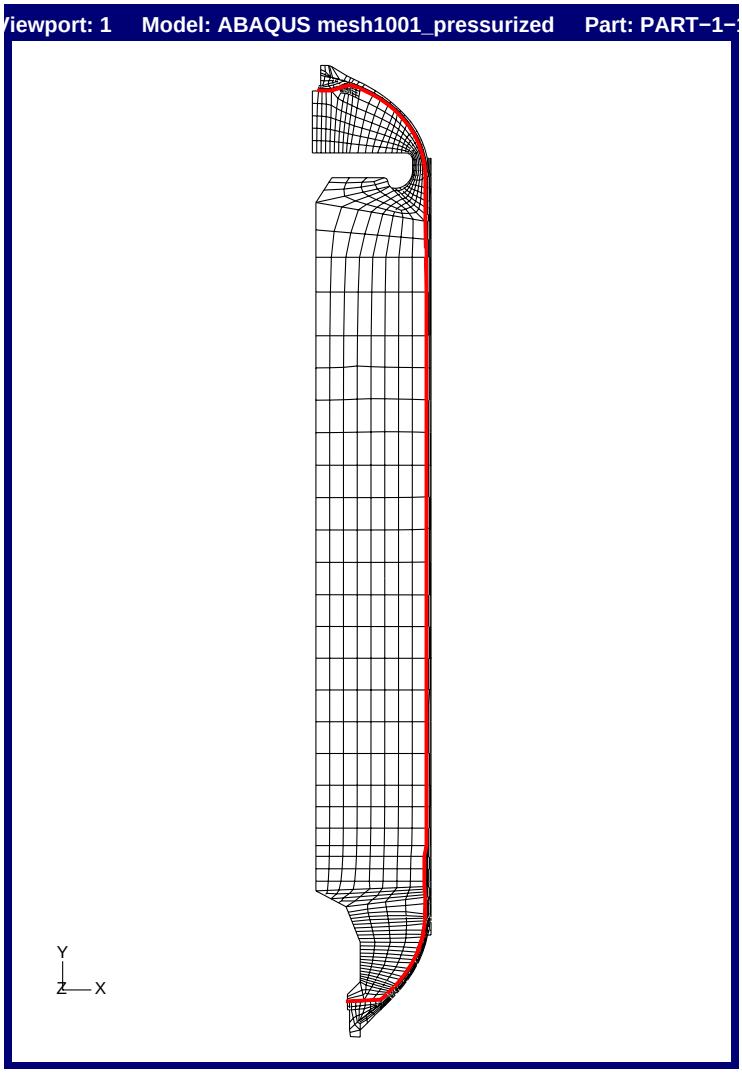

Figure A.4. Liner section in ABAQUS CAE

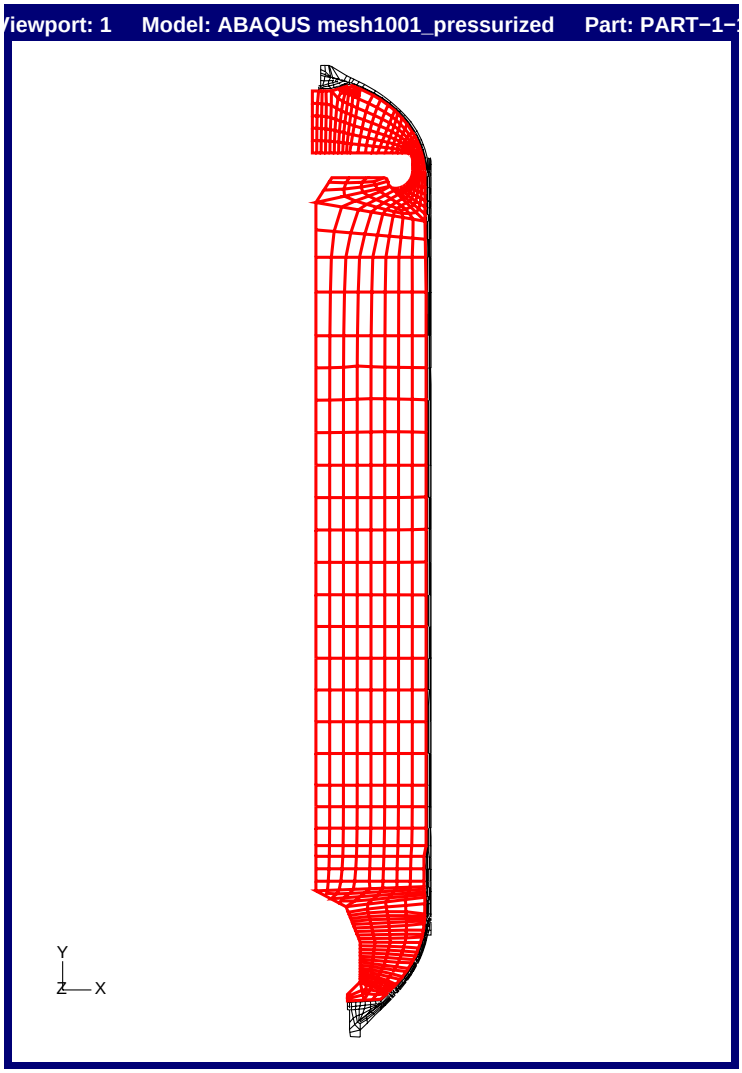

Figure A.5. Propellant section in ABAQUS CAE

APPENDIX B: UNDEFORMED AND DEFORMED VIEWS

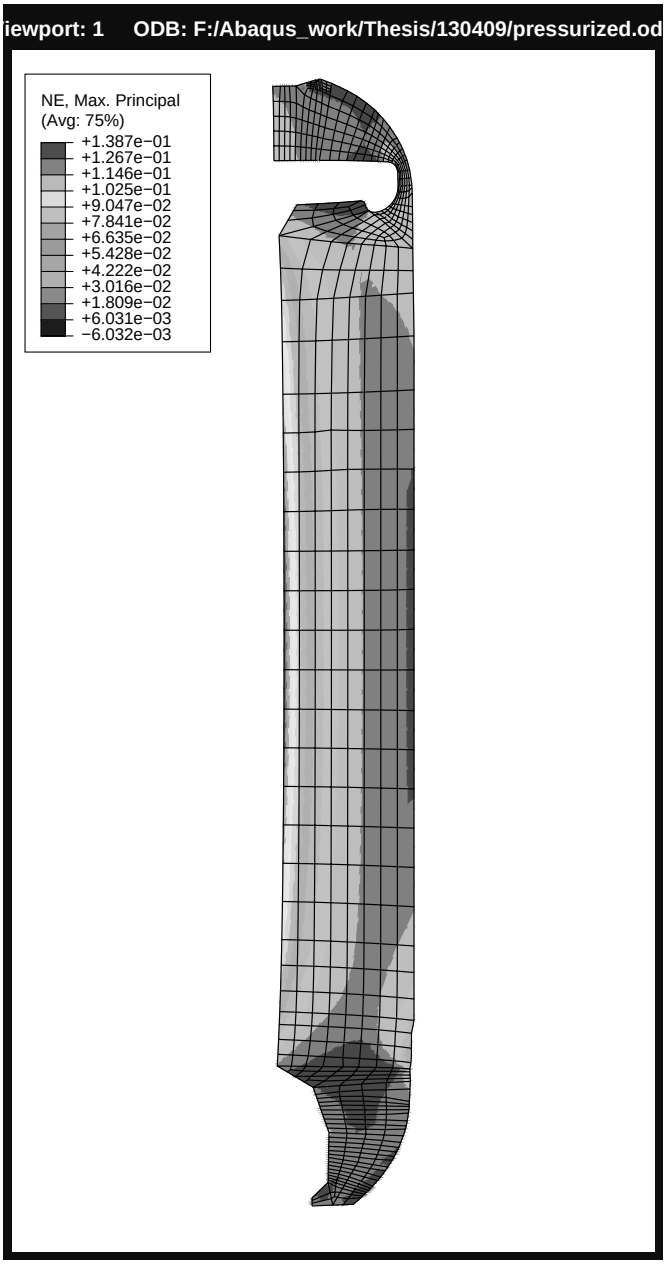

Figure B.1. Deformed view of the motor at ignition pressurization analysis

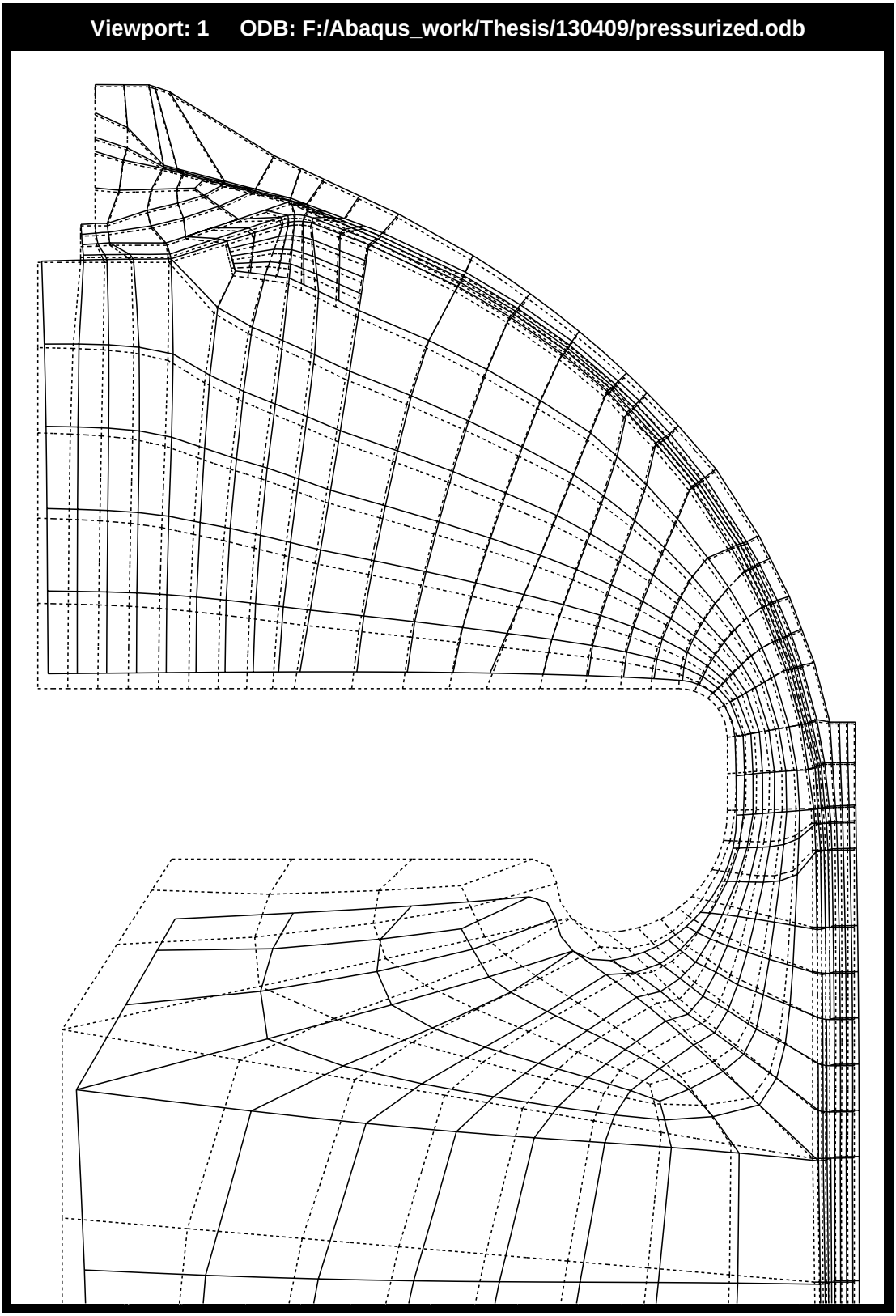

Figure B.2. Slot x

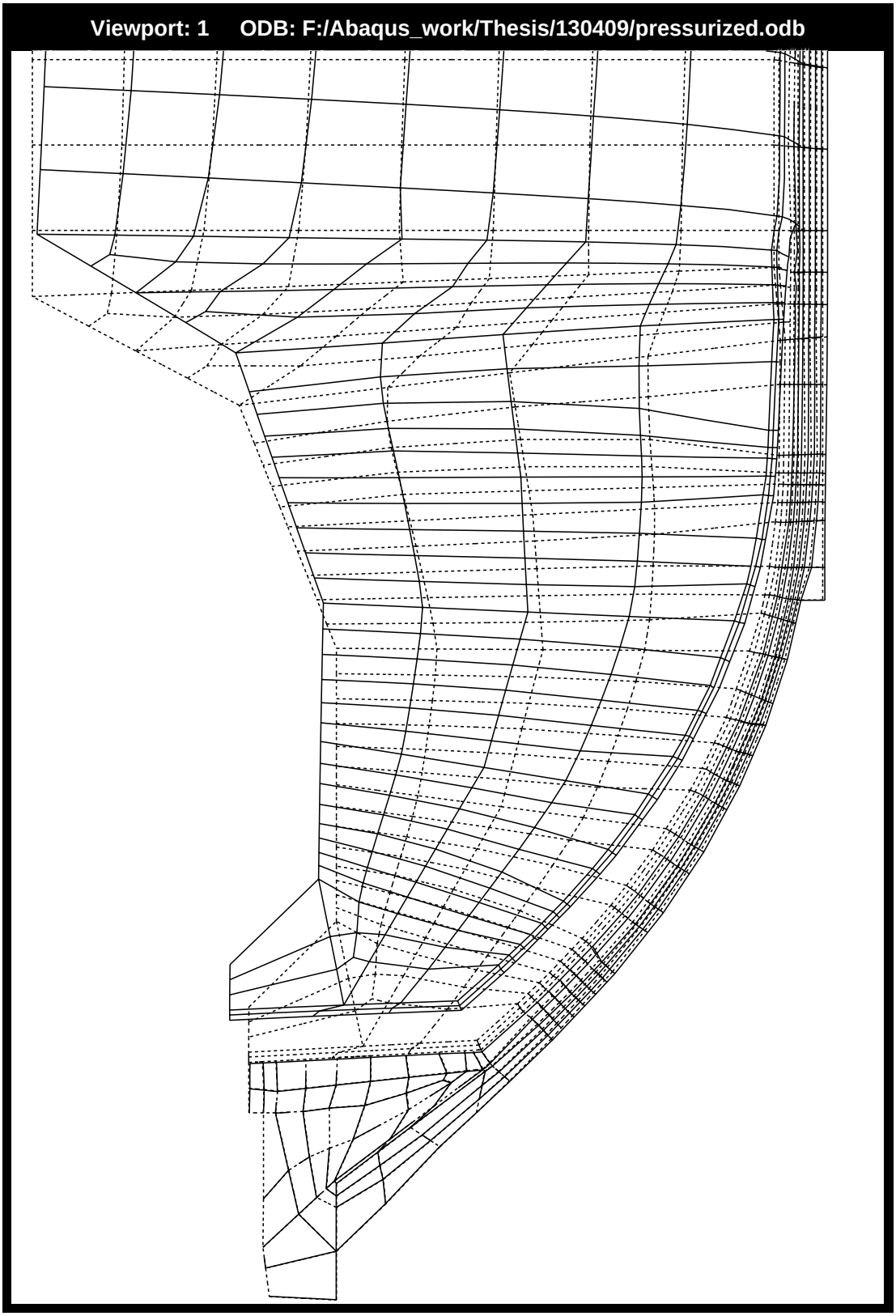

Figure B.3. Bond x

REFERENCES

1. Ho, S.Y., "Viscoelastic response of solid rocket motor components for service life assessment." *Journal of Materials Science* Vol.32, pp. 5155-5161, 1997.

2. Wadiak, D.T., P.M. Bond, N.A. Cyr, S. Fields, G.H. Ferguson and L.W. Swenson " A finite element methodology to predict age-related mechanical property and structural performance changes in high performance polymers." *International Journal for Numerical Methods in Engineering* Vol.29, pp. 1159-1175, 1990.

3. Keizers, H.L.J. and J.R. Miedema, "Structural service lifetime modelling for solid propellant rocket motors." *AGARD conference proceedings 586*, reference 32, 1997.

4. Swanson, S.R. and L.W. Christensen , "A Constitutive Formulation for High-Elongation Propellants." *Journal of Spacecraft and Rockets* Vol. 20, pp. 559-566, 1983.

5. Simo, J.C., "On a Fully Three-Dimensional Finite-Strain Viscoelastic Damage Model: Formulation and Computational Aspects." Computer Methods in Applied Mechanics and Engineering, Vol. 60, pp. 153-173, 1987.

6. Özüpek, Ş. and E.B. Becker, "Constitutive Modeling of High-Elongation Solid Propellants.", *Journal of Materials and Technology* Vol.114, pp. 111-115, 1992.

7. Özüpek, Ş., "Constitutive Equations for Solid Propellants.", *Journal of Materials and Technology* Vol.119, pp. 125-132, 1997.

8. Canga, M., E.B. Becker and Ş. Özüpek , "Constitutive Modeling of Viscoelastic Materials with Damage-Computational Aspects.", *Computer Methods in Applied Mechanics and Engineering* Vol.190, pp. 2207-2226, 2001.

9. Kivity, M., G. Hartman and A.M. Achlama, "Aging of HTPB propellant." *Amer-*

ican Institute of Aeronautics and Astronautics 41st AIAA/ASME/SAE/ASEE Joint propulsion conferance&exhibit, AIAA 3802, 2005.

10. Heller, R.A., M.P. Kamat and M.P. Singh, "Probabaility of solid-propellant motor failure due to environmental temperatures." *Journal of Spacecaft* Vol.16, 140-146, 1978.

11. Heller, R.A. and M.P. Singh, "Thermal storage life of solid-propellant motors." *Journal of Spacecaft* Vol.20, 144-149, 1982.

12. Hazim, S.Z. and R.A. Heller, "Rocket motor service life calculations based on the first-passage method." *Journal of Spacecaft* Vol.26, 279-284, 1989.

13. Collingwood, G.A., L.M. Clark and E.B. Becker, "Solid rocket motor service life prediction using nonlinear viscoelastic analysis and a probabilistic approach." *AGARD conference proceedings 586*, reference 29, 1997.

14. Chen, J.T. and S.Y. Leu, "Finite element analysis, design and experiment on solid propellant motors with a stress reliever." *Finite Element Analysis and Design* Vol.29, pp. 75-86, 1998.

15. Treloar, L.R.G., *Trans Faraday Society* ,pp. 39-241, 1943.

16. Yeoh, O.H., "Some Forms of the Strain Energy Function for Rubber.", *Rubber Chemistry and Technology* Vol. 66, pp. 754-771, 1993.

17. Özüpek, Ş., "KatıYakıtlı Roketlerin Gerilme Analizi ve Hizmet Ömrü Öngörüsü.", *TUBITAK* project number 104M269.

18. Williams, M.L., R.F. Landel and J.D. Ferry , "The temperature dependence of relaxation mechanism in amporphous polymers and other glassliquids." *Journal of the American Chemical Society*, pp. 77-370, 1955.

19. Chyuan, S.W., "Studies of poissons ratio variation for solid propellant grains under

ignition pressure loading." *International Journal of Pressure Vessels and Piping* Vol. 80, pp. 871-877, 2003.

20. Hibbit, Karlsson and Sorenson, Inc. 2007. ABAQUS User's Manual, version 6.7.

21. McDonald, A.J., "Fixing the Field Joint That Failed on the Challenger.", *Journal of Propulsion* Vol. 7, pp. 130-138, 1991.